공학박사 학위논문

Advanced Applications of Thin Film Optics using Metal-Dielectric-Metal Etalon

금속-유전체-금속 박막 에탈론 구조의 광학적 응용

2023년 8월

서울대학교 대학원

공과대학 전기·정보공학부

이 종 수

Advanced Applications of Thin Film Optics using Metal-Dielectric-Metal Etalon

지도교수 곽 정 훈

이 논문을 공학박사 학위논문으로 제출함

2023 년 7 월

서울대학교 대학원

공과대학 전기·정보공학부

이 종 수

이종수의 공학박사 학위논문을 인준함

2023 년 6 월

위 원 장 이 재 상 (인)

부위원장 곽 정 훈 (인)

위 원 유 선 규 (인)

위 원 나 준 희 (인)

위 원 유 용 상 (인)

Abstract

Advanced Applications of Thin Film Optics using Metal-Dielectric-Metal Etalon

Jongsu Lee

Department of Electrical and Computer Engineering

The Graduate School

Seoul National University

Light-matter interaction based on noble-metal nanostructure has received constant attention for its tremendous potential on scientific discovery as well as practical devices by its unique optical characteristics. Meanwhile, constructing nanostructured platform requires costly and complicated fabrication process to produce wide-range visible colors for real-world applications. In this point of view, the Fabry-Perot (FP) resonator is an intuitive and versatile optical structure for its uniqueness in light-matter interaction yielding resonance with wide-range of wavelength as it couples with photonic materials encapsulated in dielectric cavity. A simple metal-dielectric-metal (MDM) thin film stack, also known as etalon, induces FP interference capable of generating full-color coverage in visible range and exhibiting a high level of color tunability via engineering the geometry and material of comprising layers. It requires relative

cost-effective fabrication processes such as deposition and spin-coating which are beneficial for large-area mass production.

First, thin-film thickness and filling-fraction of each composition layer were precisely tailored to produce delicate color variations together with a theoretical modeling for setting a restrict standard on color guide. Through materialized experiments, a thin-film etalon with nanostructures was demonstrated to realize its unique structural coloration and also applied its color tunability to functional mimicry of environmental-sensitive optical camouflage. Second, conversion of gas-matter interaction into light-matter interaction was attempted for visualizing the dynamic gas absorption/desorption at the palladium-facing interface since palladium has a unique characteristic as a catalyst and a hydrogen absorber, which makes it the most prominent material in a wide range of gas industries including hydrogen storage, purification, detection, and catalyst. Therefore, palladium was simply utilized for the top and bottom metal layers of FP etalon to induce colorimetric reactions against exposed gas, and consequential water-forming reactions at the dielectric/Pd interfaces results in naked-eye color changes with respective of gas concentration under ambient environment. Such device was successfully demonstrated to the applicable level of a gas leakage warning system. Lastly, the MDM etalon structure was employed for advanced molecular detection technology as a 'Raman switch' that is capable of tuning the surface-enhanced Raman scattering (SERS) enhancement factor (EF). Investigation for producing the optimum near-field as well as far-field SERS EF was conducted via engineered nano-geometry of composing FP etalon with the help of

computational and experimental analyses. Such SERS tuning by modulation of structural characters of optical cavity expands its applicability for information encryption.

In conclusion, this thesis presents throughout investigation of the MDM etalon structure as a thin film optic device and suggests its various application fields including surface chemistry, heterogeneous catalysis, biomimicry and molecular analysis as well as optics. Both experimental and computational analysis were conducted to prove the optical behaviors of the etalon devices depending on their composition and nanomorphology. The strategy for introducing dynamicity inside the MDM structure can be applied to a variety of photonic nanostructures for a wider range of wavelength spectra.

Keywords: Fabry-Perot etalon, Structural color, Water-forming reaction, Colorimeter sensors, Raman spectroscopy

Student Number: 2018-35203

Table of Contents

List of Figures

Chapter 1. Introduction

Light-matter interaction encourages significant optical scattering and absorption at specific wavelengths. It has become a crucial principle in the development of advanced research including photovoltaics [1], biochemical analysis [2], nonlinear optics [3], color printing [4], and spectroscopy [5]. In particular, plasmonic devices with sub-wavelength nanogeometry exhibit meticulous optical modulation in the visible light region, thereby, evaluated as the next-generation color displaying and sensing technology. For decades, 'static plasmonic' materials/devices have led a major stream of studies, modulating optical properties over the predefined structures once incident light is exposed. Recently, new era of ‘dynamic plasmonic’ materials/devices keeps step with rapid development of artificial intelligence technology and the implementation of meta bus super-connected society, as they require a variety of information from a wide range of external stimuli such as temperature [6], strain [7], moisture [8], biochemical molecules [9], gas [10], etc.

Dynamic plasmonic technology is highly advantageous in reversible coloration and selective manipulation of light scattering/absorption in the visible spectra. These extraordinary optical phenomena, determined from the variation of constituting materials or their variables (nanostructure's shape, size, arrangement, and surrounding medium), lead to creation of electric-based color tuning technology. For example, liquid crystal technology combined with

anisotropic metal nanostructures shows active plasmonics-assisted coloration [11]. Electrochemical deposition triggers color modulation based on accumulation of metal ions in an electrolyte [12]. And hybrid electrochromic polymers under a redox reaction yield a change of complex dielectric property [13]. However, such techniques displaying chromatic modulation worked under limited environments including a liquid or quasi-liquid medium with electrical bias. Consequently, dynamic modulation platforms that can respond to not only electric-fields, but a variety of stimuli such as temperatures, pH, light, magnetic field, and solvent composition are desirable for realization of intelligent applications such as information encryption, anti-counterfeiting, and chromatic printing/sensing [14].

On the other hand, enhancing Raman scattering had a great accomplishment along with the development of nanotechnology, enabling it to detect molecular fingerprints not only for analytical research but even in daily-life practical applications. Surface-enhanced Raman scattering (SERS) on metal nanoparticles greatly concentrates the incident light and transfers the amplified energy to the nearby analytes in the orders-of-magnitude [15]. Additionally, the nano-scaled gap between metal particles has drawn great attention as “hot spot” that generates electromagnetic (EM) field enhancement, so diverse strategies to narrow the gap and concentrate the analytes within it have been achieved to enable single molecule detection with enhancement factor of $\sim 10^{14}$ [16]. Despite their detection sensitivity, the uniformity of Raman signal and easy fabrication with large-area were required for practical application.

Spontaneous forming of random nanostructures on the substrate is a well-known low-cost fabrication process for uniform SERS signal. For example, maskless reactive ion etching (RIE) often induces the re-deposition of impurities that can produce nano-pillars (micromasking effect) [17]. Subsequent Au deposition on this nano-pillars provides highly enhanced Raman signals with large-scale. In another case, the thermal dewetting of the thin metal film also generates well-controlled metal nanoparticles with easy fabrication [18]. Although the random nanostructures are cost-efficient for mass-production, it is still limited in precise control of plasmon resonance.

This thesis focuses on a MDM etalon structure with nano-perforated top metal layer which cost-effectively produces not only a wide range of structural coloration but also dynamic colorimetric sensing of refractive indices and catalytic chemical reaction, and even tunable Raman enhancing performance. Moreover, precise engineering of the etalon device suggests various functionalities to the simple colorimetric platform by determining proper geometry and kind of the composing materials.

1.1. Structural Coloration

Structural coloration refers to the implementation of color by utilizing the interference, absorption, and scattering of light from a wavelength or sub-wavelength scale nanostructure without the use of dyes or pigments. This type of coloring has been variously observed in nature such as the wings of morpho-butterflies and the skin of chameleons [19]. In addition, the Roman Lycurgus cup has been shown that the structural color based on plasmonic effects was

already used in the ancient human society [20]. For a few decades, many researchers strived for implementing various methods of structural colorations because of their advantages such as long-term stability, high reliability, efficient manipulation of visible light, and harmlessness for human body [21]. It has been known that diffraction gratings, selective mirrors, photonic crystals, and deformed matrices can be used as concrete methods to realize structural coloration [22, 23]. Indeed, these methods have been applied and developed in various fields such as bio/chemical sensors, color filters, absorbers, anti-counterfeiting stickers, and devices for optical camouflagby utilizing the distinctive characteristics of structural coloration [24-29].

However, most of the artificially made structural-colored layers which based on top-down process have inherent industrial disadvantages since they often involve complex and expensive fabrication processes such as e-beam lithography and repetitive depositions [30]. For more inexpensive process, various studies have been reported, such as using randomly deposited metal nanoparticles or nanowires [31, 32]. Among such studies, devices with randomly deposited metal layers on metal-dielectric-metal (MDM) etalon structures have also been introduced [33-35]. These structures demonstrate that the Fabry-Perot (FP) resonance existing on MDM etalons can be utilized with adjustable scattering effects of randomly deposited metal nanoparticle layers.

Inspired by the broad spectral variation reported in [35], a slight change in the fabrication process conditions could allow the metal-nanoparticle based MDM etalon to implement various structural colors. Particularly, depending on the composition ratio of the random Au-islands, this mixture layer can be either

a particle-like structure, a randomly connected network, or a film-like structure. We have examined the effects of the variation in the morphology of the Au-island mixture to the structural color generated by the proposed etalon. The verification of proposed configuration is done by comparing actual experimental results with the transfer matric method (TMM)-based simulations that approximate the mixture layer as a uniform effective material through Bruggeman's effective medium theory (BEMT).

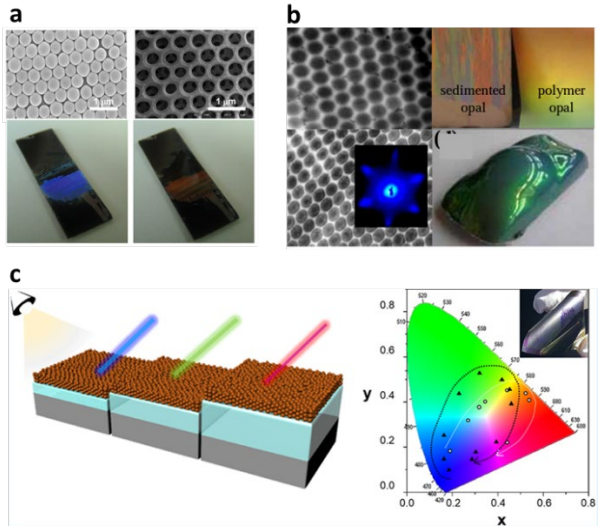

Figure 1.1: Examples of structural color generation by photonic crystals (a; reproduced from [24]), polymer opals (b; reproduced from [29]), and FP resonators (c; reproduced from [36]).

1.2. Surface-enhanced Raman Spectroscopy

The theoretical correlation between SERS enhancement factor (EF) and EM intensity of excitation and scattering light is generally known to follows the equation:

$$\mathrm{EF} = \frac{|E_{loc}(\lambda_{ex})|^2 \cdot |E_{loc}(\lambda_{sc})|^2}{|E_0|^2 \cdot |E_0|^2} \quad (1.1)$$

where $E_{\mathrm{loc}}(\lambda_{\mathrm{ex}})$, $E_{\mathrm{loc}}(\lambda_{\mathrm{sc}})$, E_0 are local electric field strength at the excitation, at scattering wavelength, and incident electric field strength, respectively [37, 38]. Advanced nanofabrication technologies have experimentally revealed the correlation between optical resonance and SERS enhancement by the precise adjustment of gap distance, feature size, and shape [39]. Moreover, the SERS substrates combined with stimuli-responsive materials opens up opportunities for new practical applications as well as an understanding about the correlation.

Due to its theoretical and experimental progress, more specialized SERS substrates have been suggested for various application fields including biochemical research [40], environmental sensing [41], food safety [42], and anti-counterfeiting [43]. Especially, the anti-counterfeiting application utilizing the SERS effect is realized through the decoding process in which the molecular information on the substrate is converted to a Raman mapping image for visualization. Therefore, it is necessary to not only satisfy general requirements for SERS application, but also to establish an encryption strategy. For example, the encrypted information can be decoded by types of probe molecules, their concentration, polarization, and focal plane dependent Raman intensity. These methods suggest that distinct Raman signals are obtained on a single substrate

according to the optical properties of nanostructures and chemical species. However, a simple and mass-production compatible platform enabling real-time Raman intensity modulation is still desired for the realization of dynamic message encryption.

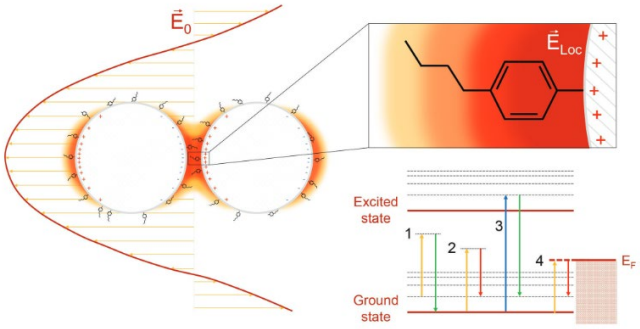

Figure 1.2: Conceptual outline of the main elements of SERS (reproduced from [37])

1.3. Outline of Thesis

This thesis represents six chapters including **Introduction**, **Theoretical Backgrounds** and **Concluding Remarks**. In **Chapter 1**, general overview of FP resonators for structural coloration and SERS is introduced with its specific fields of applications. To understand the physical and optical properties of nanostructured MDM etalons, the theoretical backgrounds about FP resonator and Raman spectroscopy are provided in **Chapter 2**. **Chapter 3** demonstrate the effects of each composing layer's physical parameters to the overall structural colors of the MDM etalon. Due to the nano-apertures of top metal layer, additional tuning of the dielectric layer is available by conventional dry etching process, and it provides dynamicity to the color of the device. In **Chapter 4**, water-forming catalytic reaction of hydrogen and oxygen gases are induced at the interface of the dielectric layer and metal layer. Such reaction shows two distinct water-forming phenomena depending on the environmental gas composition resulting different color changing behaviors. The confinement of chemical reaction inside the MDM etalon structure suggests not only a new monitoring technique of surface chemistry and gaseous reactions but also an effective gas leakage warning technology. In **Chapter 5**, the nanomorphology of top metal is utilized to induce SERS effect, and FP interference plays a role as a modulator for tunable Raman substrate. In this case, the additional tailoring of dielectric layer can also provide liquid permeability to the structure, which is used as a Raman switch turning on/off its Raman signal. At the end, **Chapter 6** summarizes the overall thesis and envisions future applicability of MDM etalons.

Chapter 2. Theoretical Background

2.1. Fabry-Perot Optical Resonator

In 1899, Charles Fabry and Alfred Perot have developed an optical resonator consisting of two parallel semitransparent metal mirrors separated by an optical spacer [44]. This interferometer, or etalon, manipulate light of specific wavelength by controlling its resonance. Both transmissive and reflective interpretations are available as described in Fig. 2.1. As the incident light (E_0) partially reflects and transmits at the first mirror, the transmitted light undergoes multiple reflection and transmission at the optical cavity. According to TMM [45],

$$\begin{bmatrix} \boldsymbol{E}_R \\ \boldsymbol{E}_0 \end{bmatrix} = \begin{bmatrix} \mathrm{M}_{11} & \mathrm{M}_{12} \\ \mathrm{M}_{21} & \mathrm{M}_{22} \end{bmatrix} \begin{bmatrix} \boldsymbol{E'}_0 \\ \boldsymbol{E}_T \end{bmatrix} = \mathbf{M} \begin{bmatrix} \boldsymbol{E'}_0 \\ \boldsymbol{E}_T \end{bmatrix} = \mathbf{M}_1 \mathbf{M}_2 \mathbf{M}_3 \begin{bmatrix} \boldsymbol{E'}_0 \\ \boldsymbol{E}_T \end{bmatrix}, \qquad (2.1)$$

where E_0, E_R, E_T and E'_0 are wave functions of incident light, reflected light, transmitted light, and light from the other side, respectively. The transfer matrix, $\mathrm{M_m}$, for each layer is as follows,

$$\mathbf{M}_m = \begin{bmatrix} \cos\left(k_m d_m\right) & -\dfrac{i}{k_m}\sin\left(k_m d_m\right) \\ -ik_m \sin\left(k_m d_m\right) & \cos\left(k_m d_m\right) \end{bmatrix} \quad m = 1,2,3\,. \qquad (2.2)$$

where d, ε, and k are thickness, permittivity, wavenumber of layer m. Since we are interested in a three-layer-system, the coefficient of reflection (r) and transmission (t) is given by,

$$r = \frac{k_0 \mathrm{M}_{11} + k_0 k_T \mathrm{M}_{12} - \mathrm{M}_{21} - k_T \mathrm{M}_{22}}{k_0 \mathrm{M}_{11} + k_0 k_T \mathrm{M}_{12} + \mathrm{M}_{21} + k_T \mathrm{M}_{22}} \tag{2.3}$$

$$t = \frac{2k_0}{k_0 \mathrm{M}_{11} + k_0 k_T \mathrm{M}_{12} + \mathrm{M}_{21} + k_T \mathrm{M}_{22}}. \tag{2.4}$$

Based on these coefficients, reflectance (R) and transmittance (T) can be calculated by $R = |r|^2$, $T = |t|^2$, and $R + T + A = 1$ where A is absorption.

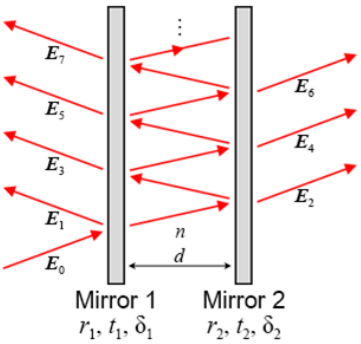

Figure 2.1: Schematic description of FP optical resonator, reproduced from [46].

2.2. Bruggeman's Effective Medium Theory

Instead of calculating full electromagnetic solution of proposed randomly distributed configuration, TMM solution of simplified one-dimensional (1D) multiple thin film stacked model was applied. The Au/air mixture layer is assumed as homogeneous effective medium based on BEMT which gives an effective permittivity of random mixture of two distinct materials with sub-wavelength scale morphology. The effective permittivity can be achieved by solving the following equation:

$$f_1 \frac{\varepsilon_1 - \varepsilon_{mix}}{\varepsilon_1 + \kappa\varepsilon_{mix}} + f_2 \frac{\varepsilon_2 - \varepsilon_{mix}}{\varepsilon_2 + \kappa\varepsilon_{mix}} = 0. \quad (2.5)$$

Here, ε_i (i =1, 2) and f_i (i =1, 2) are the permittivity and the volume filling fraction of each constituent material in the mixture, respectively. κ is related to Lorentz depolarization factor, which varies from κ = 1 for 2D mixture to κ = 2 for 3D case [47]. In this case, κ is 1 since the thickness of the layer is much smaller than optical wavelength in visible range.

2.3. Raman Spectroscopy

In 1928, an Indian physicist, Chandrasekhara Venkata Raman discovered an inelastically scattered radiation known as Raman scattering. When a monochromatic radiation is incident on a matter, both Rayleigh scattering having the same frequency of the incident light and Raman scattering having different frequency occurs [48]. This frequency shift of Raman effect happens by the excited molecular vibration energy. Figure 2.2 shows two types of

spontaneous Raman scattering: Stokes scattering (frequency redshift) and anti-Stokes scattering (frequency blueshift). Coherent anti-Stokes scattering can be observed when the sample is initially excited. Raman spectroscopy measures the frequency shift which depends on the chemical composition of the molecules. Therefore, it is a specialized technique to obtain the fingerprints of analytes with the great advantages of remote and real-time sensing.

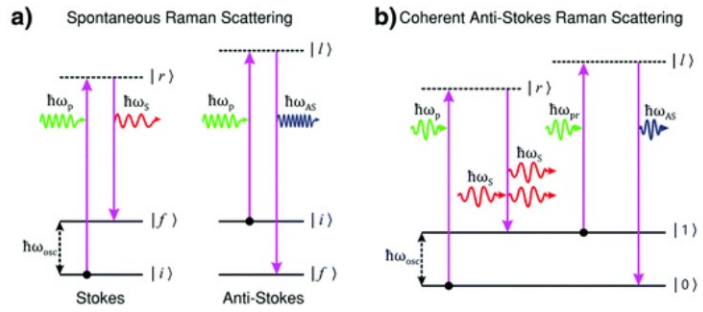

Figure 2.2: Schematic description of Raman scattering, reproduced from [48].

Chapter 3. Full-colored Structural Coloration with Thin-film Etalon Composed by Gold-nanoparticle Effective Medium

3.1. Introduction

Fabrication of micro- or nano-structures for structural-coloration through top-down processes is fundamentally unfavorable in manufacturing aspects because it requires complicated and highly expensive techniques which obviously have restricted scalability and mass production. In opposition, bottom-up processes can overcome those limitations and achieve structural-coloration using relatively simple and cost effective metal deposition processes or spreading randomly-dispersed metal nanoparticles having subwavelength scales [31, 32, 35]. In this aspect, a device that confines specific wavelengths of incident light within a metal-dielectric-metal (MDM) stack demonstrated unique opportunities in color displays by taking advantage of an optical phenomenon called Fabry-Perot (FP) resonance or Mie scattering [33, 34, 36, 49-51]. In addition, a color modulator using enhanced Mie scattering with lattice resonance has also been reported [52]. Previously, a reflective liquid-permeable MDM etalon was demonstrated for refractive index (RI) sensor working in the visible region with the record high color shift value of 323.5 nm/RIU, depending on the RI of the infiltrated solution [35]. However, an achievement of high-level of color tunability without covering full-colored visible range is

insufficient to satisfy its availability for practical real-world application. Besides, establishment of a color guide map of MDM stack with delicate control of its constituents is highly desirable.

3.2. Basic Concept

In this chapter, a full spectrum of structural colors with a thin-film etalon is introduced consisting of a uniform film of transreflective Au, perfluoro-(butenyl vinyl ether) (PBVE) polymer dielectric film, and bottom reflective Au from the top to bottom. The roles of geometrical features of each layer on the device's coloration were examined by varying their thickness and filling-fraction (i.e. top Au and PBVE films). Based on theoretical modeling coupled with experimental verification, we established color guide maps of the MDM etalon, which was further applied to functional mimicry of optical camouflage for environmental-sensitive color display. Figure 3.1 shows the conceptual schematic of the proposed Bruggeman effective etalon reflecting various light colors in broad range depending on physical properties of comprising films, such as dielectric layer thickness ($t_{\text{dielectric}}$) and volume filling fractions of top metal (f_{metal}) and dielectric layer ($f_{\text{dielectric}}$). To test proposed conceptual optical color variation, we prepared MDM stack consisting of 100-nm-thick Au on Si substrate (as full reflector), and PBVE as a polymer layer (as optical cavity), and Au/air mixed top layer (as transreflective metal film) from bottom to top. A deposition of metal atoms on dielectric surface results in randomly-distributed metal/air mixed layer producing the f_{metal}, and resultant values of the f_{metal} can be engineered varying deposition conditions such as time, rate, and

pressure or surface energy of dielectric layer.[35, 51] Throughout the chapter, the physicochemical roles of both top- and PBVE layers were examined since they are proven to significantly contribute to structural coloration of MDM structure.

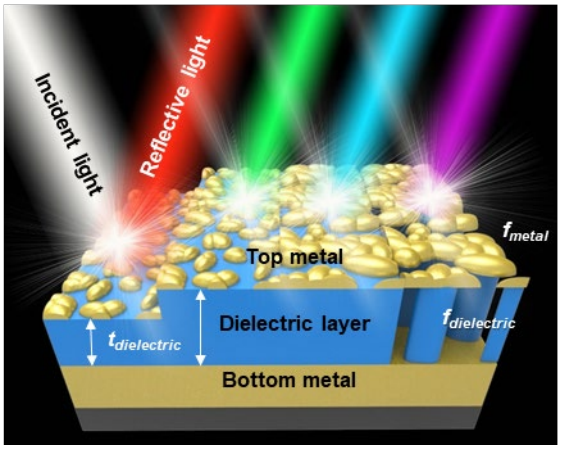

Figure 3.1: Schematic illustration of proposed MDM stack varying configuration of composing materials.

3.3. Experiments

3.3.1. Fabrication of Au-PBVE-Au etalon

The bottom reflection layer was prepared by depositing 10 nm Ti adhesion layer followed by 100 nm Au film on Si substrate using a thermal evaporator (MHS-1800, Muhan; 10^{-7} Torr; 2.0 Å/s). Dielectric films with various thicknesses (d = 110, 135, and 165 nm) were achieved by spin-coating the mixture solution [9.0 wt. % PBVE (Chromis Technology) with solvent (FC-43, Chromis Technologies) in ratio of 1:1] at controlled spinning rates (7200, 4400, and 3000 rpm for 45 s, respectively), followed by baking process on hotplate at 80 °C for 1 h. Thickness of PBVE was locally reduced using RIE (RIE 80 plus, Oxford Instrument), and its surface energy was relieved by annealing on hotplate at 180 °C for 2 h. O_2 plasma surface treatment was performed on PBVE surface to obtain high f_{PBVE}. The Bruggeman effective medium geometry of top Au layer was slowly deposited on PBVE (10^{-7} Torr, 0.3 Å/s). Finally, additional RIE was performed to create dielectric cavity. More detailed fabrication steps of demonstration discus fish sample is in Figure 3.2.

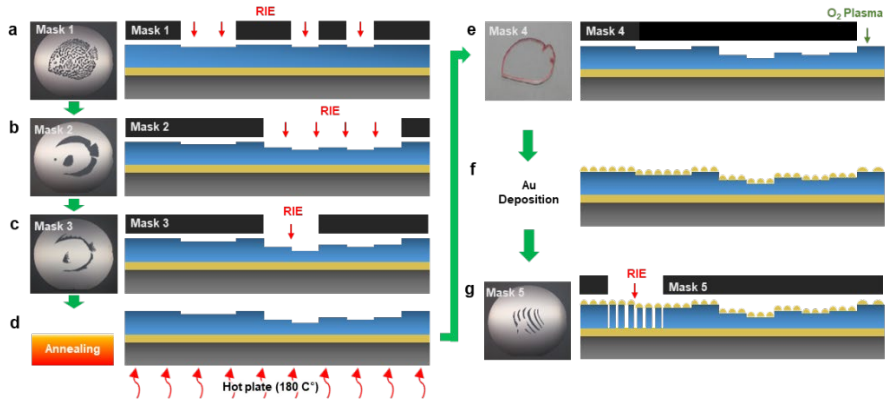

Figure 3.2: (a-g) Schematic illustration of etching and surface treatment processes of discus fish sample fabrication. Steps (a-c) and (g) are etching processes with different shadow masks. (d) Annealing process on hot plate (180 °C) to relieve PBVE's surface energy. (f) Low-density nucleation deposition of Au using a thermal evaporator.

3.3.2. Reflectance spectrum measurement

Guided through an optical fiber reflection probe (R400-7-SR, Ocean Optics), white light from a deuterium and tungsten-halogen light source (DH-MINI, Ocean Optics) was incident on the sample in a normal direction. Then, normally reflected light was guided into an ultraviolet-visible spectroscopy (USB4000-UV-VIS, Ocean Optics) with its spectral measurement ranging from 200 to 850 nm. During the measurements, reflectance spectra were normalized using an aluminum standard mirror (STAN-SSH, Ocean Optics). More detailed measurement set-up is in Fig. 3.3.

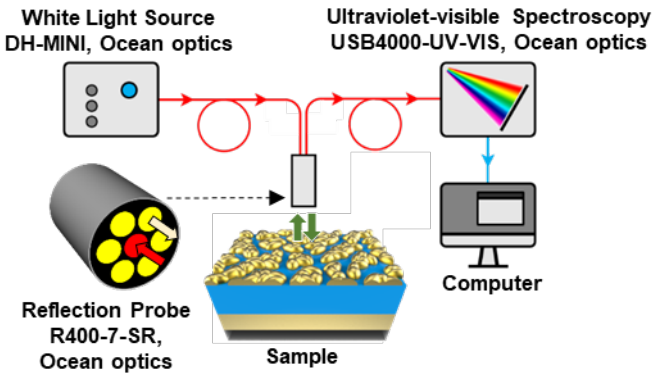

Figure 3.3: Schematic diagram of reflectance spectrum measurement. At the lower-left corner, the reflection probe is schematically illustrated as having one input terminal for reflected light that is surrounded by six output terminals for white light emission.

3.4. Results and Discussions

3.4.1. Nanomorphology of Top Au

To examine the role of the Au/air mixed layer in color variation, the BEE were produced in different f_{Au} and t_{Au} (Fig. 3.4). Four cases of controlled metal deposition conditions (identical values of rate: 0.3 Å/s, chamber pressure: 10^{-7} Torr, and θ_{BPVE}: 115° while the deposition time varies for the Cases A-C). The top- and side-view of the scanning electron microscope (SEM) images confirmed that low density nucleation of Au vapor on hydrophobic PBVE surface created particle-like Au layer with different t_{Au} and f_{Au} values. For Case D, the enhanced surface energy over PBVE surface were applied via O_2 plasma treatment to increase f_{Au} (θ_{PBVE}: ~108°) while maintaining the identical t_{Au} as the Case C (Fig. 3.5). Results obviously demonstrated that controlled deposition conditions such as deposition time (Cases A-C) and underlying surface energy (Case C) yields different f_{Au} and t_{Au}.

RIE to reduce the thickness of PBVE eventually increases its surface energy, which would prevent low density nucleation of Au vapor during the thermal deposition process. As the result, the contact angle, θ, of 10 uL DI water droplet on PBVE decreased from 115° to 78° after 36 s of RIE. To relieve and recover the original surface energy of PBVE, it was annealed at 180 °C for 2 h, and the contact angle returned back to 113°. Slight modification of its surface energy to achieve relatively high fill factor of top Au was made by O_2 plasma treatment, resulting contact angle of 108°.

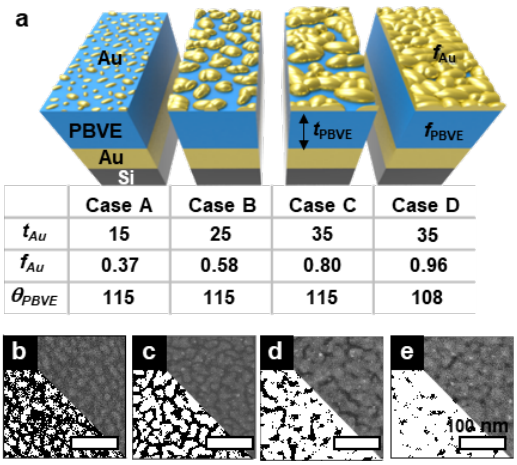

	Case A	Case B	Case C	Case D
t_{Au}	15	25	35	35
f_{Au}	0.37	0.58	0.80	0.96
θ_{PBVE}	115	115	115	108

Figure 3.4: (a) MDM structure is composed of Si substrate, 100 nm thick reflective Au film, PBVE and Au/air mixture layer with various thickness in bottom to top order. (b)-(e) top view SEM image of the structure which have Au/air mixed layer t_{Au}/f_{Au} of 15 nm/0.37, 25 nm/0.58, 35 nm/0.80 and 35 nm/0.96 from (b) to (e).

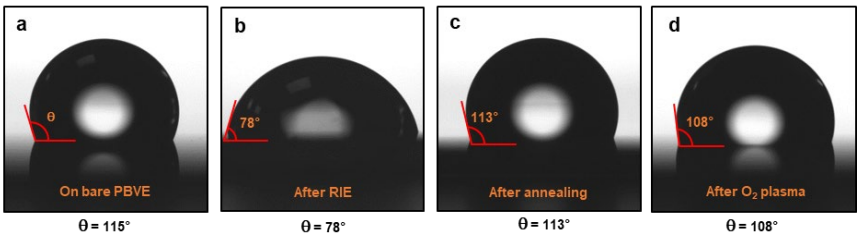

Figure 3.5: Surface hydrophobicity of PBVE. (a-d) Microscopic images of 10uL of DI water droplets on the PBVE layer after each surface treatment process with measured contact angles.

3.4.2. Colormap simulation of MDM etalon

Based on the values obtained from experiments, numerical simulations were conducted using BEMT model to investigate the influence of physical parameters (i.e., f_{Au}, t_{Au}, and t_{PBVE}) on the coloration of each MDM configuration. Figures 3.6 illustrates the calculated reflective colors where f_{Au} ranges from 0 to 1 and t_{Au} from 0 to 70 nm when t_{PBVE} is 110, 135, and 165 nm. The result indicates that $f_{Au} < 0.2$ is incapable of producing variations in structural colors implying that the reflective colors under low $f_{Au} < 0.2$ is insufficient to yield color variations due to high portion of light transmission, losing its identity as an etalon. Thus, the reflective color from bottom Au film is dominantly observed due to the transparency of PBVE. To verify the accuracy of the simulation model, calculated reflection spectra and corresponding colors were directly compared with experimental results (Fig. 3.7).

In Fig 3.7, the increase in t_{PBVE} directly red-shifts the FP resonance conditions, which is predicted from Airy formula for thin-film interference in-film interference. Hence, the location of FP resonance can be arbitrarily designed by precisely tuning t_{PBVE}. Then, the spectral variations in Cases A to D suggest that f_{Au} is strongly correlated to the sharpness and location of the FP resonance dip, which becomes narrower and blue-shifted. All of these observations can be explained by varying the effective permittivity in the mixed Au/air layer. As the f_{Au} increases, the layer becomes more metallic causing an increase in the imaginary part of the effective permittivity. This essentially increases reflections inside the etalon, which means the Q-factor of MDM

etalon becomes larger so that resonance dip becomes stronger and sharper. Moreover, variations in the effective permittivity of mixed Au/air layer affects the phase of reflection coefficient between PBVE and mixed Au/air layers resulting in the shift of the resonant wavelength condition.

In Fig. 3.6c, it is worth noting that color variation becomes subtle when t_{PBVE} = 165 nm compared with t_{PBVE} = 110 nm or t_{PBVE} = 135 nm. Such optical behavior is attributed to the shift in the resonant wavelength of the etalon from the visible to the infrared band (Fig. 3.7). When $f_{Au} < 0.8$, the resonance dip becomes much broader than the film-like top layer, and thus, wider resonance dips are expected to appear in the infrared band barely inducing visible color variation. On the other hand, in the case of $f_{Au} > 0.8$, a sharp resonance dip in the wavelength range near 630 nm is observed. As a consequence, the proposed etalon displays green color by absorbing red spectrum.

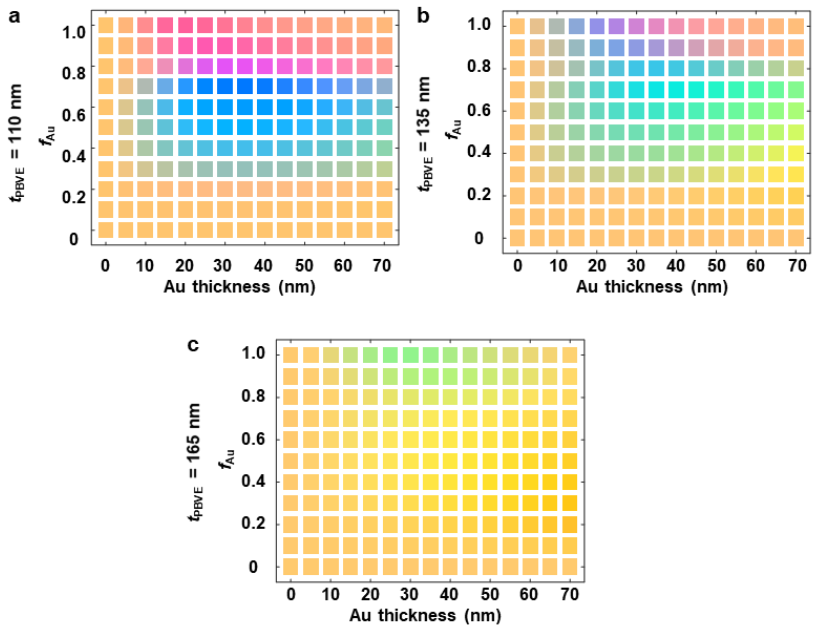

Figure 3.6: Simulated reflective color maps of the MDM etalon with (a) 110, (b) 135, and (c) 165 nm t_{PBVE}, depending on various Au/air mixed layer condition. Variables, f_{Au} and t_{Au}, are swept from 0 to 1.0 with 0.1 interval and from 0 nm to 70 nm with 5 nm interval, respectively.

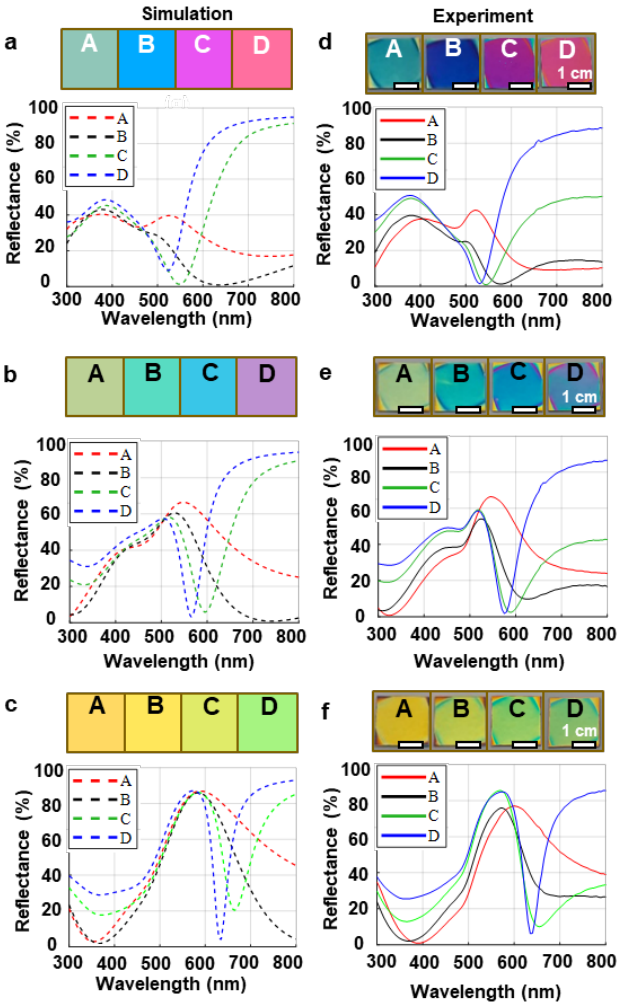

Figure 3.7: (a-c) Simulated reflectance spectra and extracted colors. (d-f) Experimentally measured reflectance spectra of the fabricated etalon samples (photographs on top; Scale bars: 1 cm).

3.4.3. Optimum Top Au Thickness for Wide Color Coverage

Having established the roles of f_{Au} and t_{PBVE} on the generation of structural colors, we now investigate the role of t_{Au} with respect to color coverage. Figure 3.8 shows simulated structural colors as a function of f_{Au} and optical path length of PBVE layer ($n_{PBVE} \cdot t_{PBVE}$), the values of which range from 0 to 1 and from 100 nm to 250 nm at t_{Au} = 10 nm, respectively. Similarly, it displays color guide maps via the proposed MDM etalon when t_{Au} = 30, 50, and 70 nm, respectively. Direct comparison of the color guides indicates that the hue of colors are mainly determined by the variation of f_{Au} and optical path length of PBVE layer, but the color saturation seems to have an optimized value determined by t_{Au}. To quantify this optical property, the CIE1931 color space was adopted, onto which the resultant colors from the color maps were marked. From the results, the widest range of color variation as well as most distinguishable color change is expected at t_{Au} = 30 nm. It is also shown that for thinner top Au layer transmission of incident light is more dominant than reflection, and thus leads to higher probability of Au-like color appearance compared to MDM etalons having thicker top Au layers. The thicker the top Au becomes, the more the light is reflected and the higher the portion of FP resonance occurs in the optical cavity. The color guides (Figs. 3.8a-3.8d) and distribution of color marks (Figs. 3.8e-3.8h) suggest that the optimum thickness for distinguishing color variations is found near t_{Au} = 30 nm.

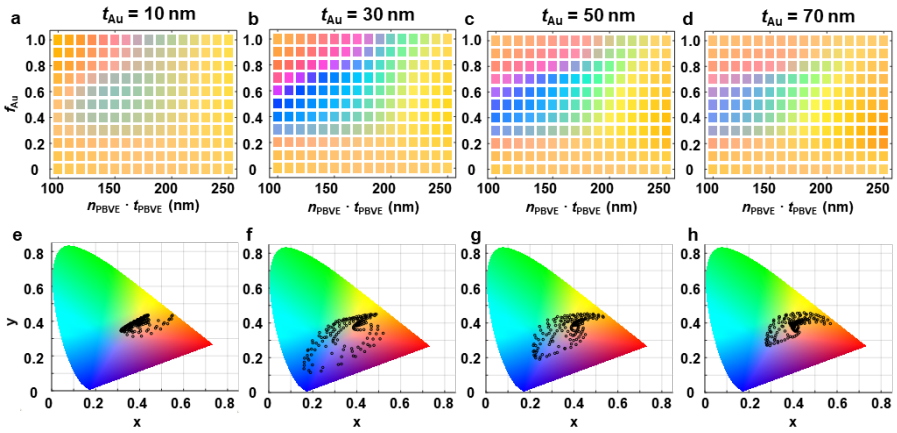

Figure 3.8: (a-d) Simulation results of colors that can be obtained by changing the structural condition of proposed etalon. In each figure, the structural condition is that f_{Au} is changed from 0 to 1.0 with 0.1 interval and optical path length of PBVE layer ($n_{PBVE} \cdot t_{PBVE}$) is changed from 100 nm to 250 nm with 10 nm interval at fixed t_{Au} of (a) 10 nm, (b) 30 nm, (c) 50 nm, and (d) 70 nm. (e-h) CIE1931 color maps with marks of all colors obtained from (a)-(d) in the same column.

3.4.4. Tailoring Dielectric Layer via Reactive Ion Etching

In contrast to other MDM etalons that completely passivate the dielectric layer with a top metal film, the proposed structure allows for tailoring of the underlying PBVE layer via RIE through the nanoscale apertures of the top Au layer (Fig. 3.9). Since the upper Au layer functions as a mask, this unique feature offers an opportunity to manipulate structural colors in a controlled manner. Figure 3.9b shows cross-section images of the samples which have undergone 0, 20, 40, and 60 s of RIE with resulting f_{PBVE} values of 1.00, 0.76. 0.51 and 0.18, respectively. The physicochemical properties of the dielectric layer mixed with PBVE nanopillars and air can also be modeled as a homogeneous layer through BEMT, analogous to the mixed Au/air films. Such additional etching procedure on the PBVE layer lowers its permittivity close to air, reducing its optical path length and imparting liquid permeability to the device since the effective refractive index of etched PBVE layer (n_{eff}) gradually decreases from $n_{PBVE} = 1.34$ to $n_{air} = 1$ (where n refers the refractive index of the material in its subscript) based on the relation made by Eq. (2.5) and subscript material. Figure 3.10a shows the simulated color change depending on $n_{eff} \cdot t_{PBVE}$ at $f_{Au} = 0.80$ and $t_{Au} = 35$ nm. Three arrows pointing to the left represent cases where $n_{eff} \cdot t_{PBVE}$ are 147, 181, and 220 nm each and their corresponding color shifts by RIE. It is shown that increasing etching time results in the shortening the effective t_{PBVE}. Figures 3.10b-3.10d show the experimental colors of the MDM etalons which were divided into four

differently-etched regions with etching period of 0, 20, 40, and 60 s, respectively. Color matching between the simulated and measured data confirmed that infiltration of air into PBVE layer tunes the dielectric property of the device. Now the etched etalons were immersed into methanol ($n_{methanol}$ = 1.34) to test additional color tuning of the etched regions to be matched with the non-etched PBVE (n_{PBVE} = 1.34) regions (Figs. 3.10e-3.10g). Such optical camouflage phenomenon can be explained by infiltration of index matching solvent to the hollow area of dielectric layer [35].

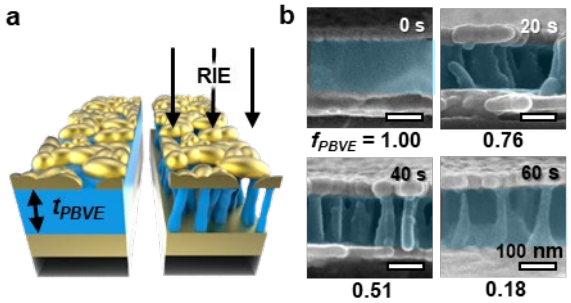

Figure 3.9: **.** (a) Schematic cross section of a MDM etalon before and after RIE. (b) Cross-sectional SEM images of the etalon samples with different f_{PBVE} (1.00, 0.7, 0.51, and 0.18) from varying etching time (0s, 20s, 40s, and 60s, respectively). Note the dielectric layer is pseudo-colored for clear recognition.

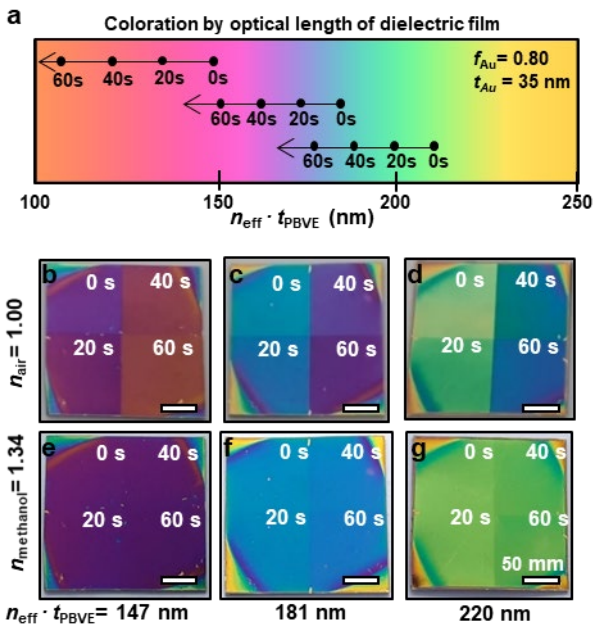

Figure 3.10: (a) Simulated color map of the proposed structure depending on $n_{eff} \cdot t_{PBVE}$ where f_{Au}= 0.80 and t_{Au}= 35nm. Indicated marks represent the color change by corresponding RIE etching times. (b-g) Photographs of fabricated samples with different $n_{eff} \cdot t_{PBVE}$ and etching times (b-d) in air (n_{air} = 1.0) and (e-g) in methanol ($n_{methanol}$ = 1.34).

3.4.5. Multiple Colors for Environmental Function Mimicry

Through all of these variables for generating a wide range of structural colors, multiple colors were tested on a single MDM etalon sample through a series of surface energy modification technique together with dielectric etching processes prior/post to the top metal deposition for dielectric change of optical path length controls (Fig. 3.11a). After establishment of the color guideline via controls of physical factors (f_{Au}, f_{PBVE}, t_{Au}, and n_{eff}) of the etalon, the color properties were applied for 'information encryption' using the optical camouflage. To make a thickness difference of the PBVE layer, the bulk PBVE film was spatially etched with controlled etching duration prior to the top Au deposition, followed by an additional annealing at 180 °C (above the glass transition temperature of PBVE, 108 °C), which is known to restore the original surface energy of PBVE after RIE process [53]. Next, O_2 plasma mildly enhanced the surface energy of the red dashed boxed area in Fig. 3.11b, resulting f_{Au} of 0.98 after Au deposition (Fig. 3.11c), whereas the black dashed region shaded by a mask produced f_{Au} of 0.86 (Fig. 3.11d). Finally, the bottom half of the sample was exposed to additional RIE to form dielectric air pockets. Figures 3.11e and 3.11f obviously show the PBVE nanopillars with different thicknesses (blue dashed region with t_{PBVE} = 165 nm while green one with t_{PBVE} = 175 nm). Moving forward, this technique was applied to a more complicated layer configuration of MDM etalon to demonstrate functional mimicry of

discus fish whose appearance is changed in response to changes in the environmental conditions.

Figure 3.12 shows 8 different sections with different structures and corresponding layer information, simulated colors, and experimental colors used to visualize a discus fish pattern. The resulting sample in Fig. 3.12b has vertical line patterns in the body region, inspired by discus fish's camouflage ability to blend in with its surrounding tree roots (left inset). The cross section of the red dashed line (Fig. 3.12b) follows the order (A to A') of the schematic structure in Fig. 3.12a. Interestingly, the proposed etalon shows highly sensitive infiltration characteristics according to the surface tension of the solution. While water (n_{water}=1.34) on the fish-patterned sample did not show any distinguishable change, the vertical patterns disappeared when it was immersed in methanol ($n_{methanol}$=1.34) (Fig. 3.12c) which even has the same RI value of water but affects much more environmentally hazardous to ecosystem. Such demonstration of environmental sensitive structural color change (Fig. 3.13) based on selective liquid infiltration into the air pockets of PBVE layer emphasizes advantages of the proposed MDM etalon which is prepared based on the physicochemical understanding of the fabrication procedures.

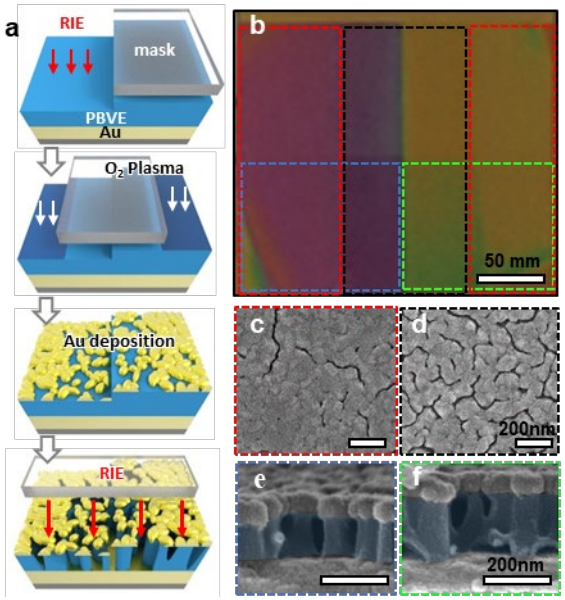

Figure 3.11: (a) Schematic description of the sample fabrication process. (b) Photograph of the resulting sample. (c-f) SEM images showing top surfaces of dashed red box area and dashed black box area and cross sections of dashed blue box area and dashed green area from (b), respectively.

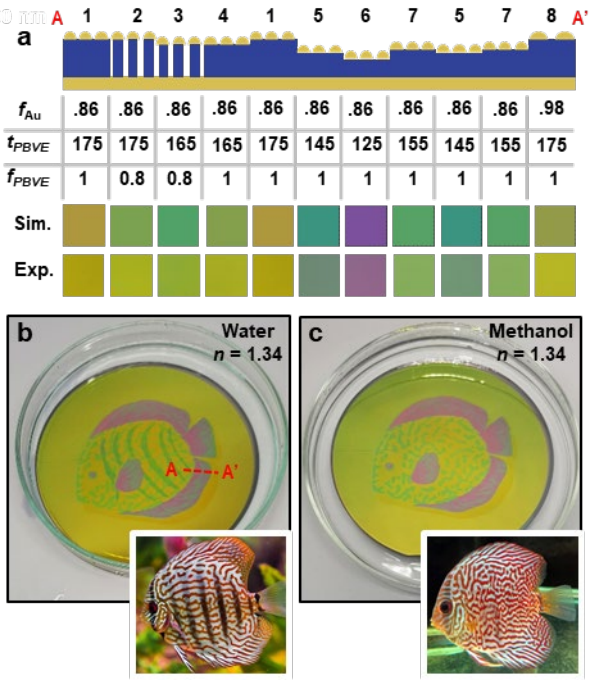

Figure 3.12: (a) Schematic cross-sectional layer information of the discuss fish demonstration sample with measured f_{Au}, t_{PBVE}, and f_{PBVE} followed by corresponding simulated colors and observed microscopic images. (b, c) Photographs of the demonstration sample in air (n_{air} = 1.00) and methanol ($n_{methanol}$ = 1.34) with insets showing photographs of a real-world discus fish with/without stripes (left/right, respectively). The red dashed line represents the cross-sectional position of (a)

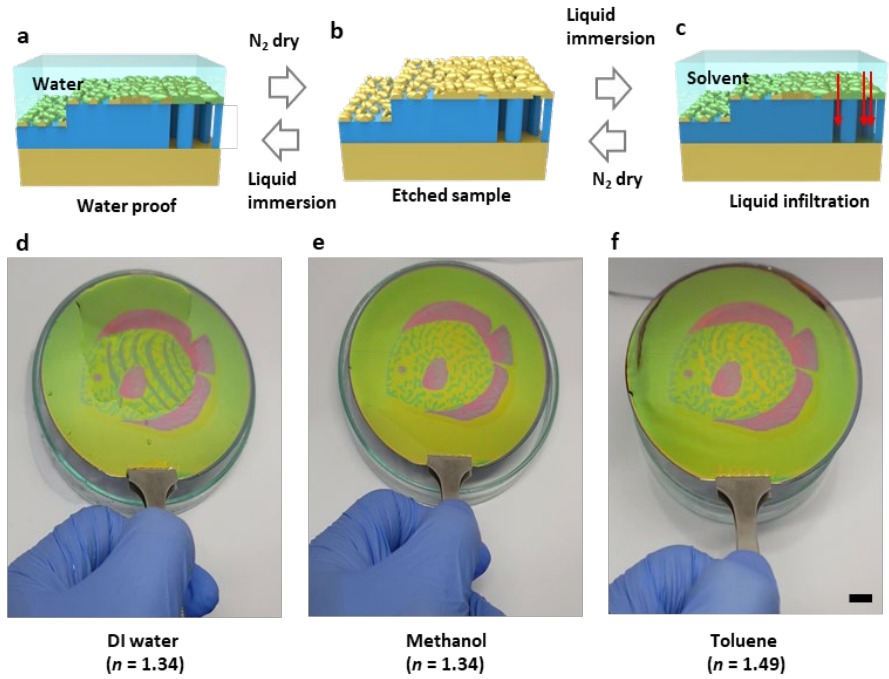

Figure 3.13: (a-c) Schematic description and (d-f) photographs of a BEE in various medium. Water does not infiltrate into the hollow insulator area, remaining the original color of the sample as shown in (d). Between each medium change, the liquid is dried by N_2 blowing, showing its reversible functionality. Organic solvent is easily infiltrate into the hollow area and changes the color of fish's stripe depending on *n* of the solvent.

3.5. Summary

Through understanding of physical variables of the MDM etalon for the generation of structural colors, a wide spectrum of colors can be realized in a single device utilizing nanostructures over a large area with simple and scalable fabrication processes. Since the thickness variation of transparent dielectric layer itself is incapable of showing visible color difference without existence of the top Au layer, the proposed technique can be applied for multichromatic image encryption as well as simple message encryption by utilizing FP resonator. Also, its liquid permeability through the dielectric cavity makes it useful for real-world applications not only in a refractive index sensor but also in the demonstration of an optical camouflage with fast response and reproducibility. The research work in this Chapter was published in [54].

Chapter 4. Naked-Eye Observation of Water-forming Reaction on Palladium Etalon: Transduction of gas-matter interaction into light-matter interaction via Palladium

4.1. Introduction

As climate change and indoor air quality management become paramount, dynamic plasmonic coloration by gas exposure is emerging as a vital future technology. Generally, gas adsorption onto metal oxides or polymers can trigger charge trapping, which induces global or local electron density changes [55]. Although reduction-oxidation reaction [56] or metal phase transitions including metal hydrides (MH_X) [57, 58] by gas absorption can shift the reflectance spectra, it is challenging to modify significant dielectric properties to reach dramatic coloration. In addition, direct tracking of an underlying atomic rearrangement and a reaction pathway in the course of gas-matter interactions is impossible in the visible spectra. This is because the feature size of such reaction components must be comparable to the resolution of the monitoring equipment: length scale-mismatching. Alternatively, extensive efforts for tracking the atomic/molecular interaction have been established by either computational simulations such as density functional theory (DFT) [59] or experimental proofs. Extravagant but state-of-the-art imaging techniques including scanning photoemission microscopy (SPM) [60], low-energy

electron microscopy (LEEM) [61], ellipso-microscopy for surface imaging (EMSI) [62], reflection anisotropy microscopy (RAM) [63], transmission electron microscopy (TEM) [64], and their multiple combinations are the examples. However, such atomic-level observations can be visualized if atomic gas-matter reactions can be translated into light-matter interactions, which can remove the stringent restrictions of state-of-the-art measurement techniques. Thus, one could circumvent the diffraction limit of measurements by bypassing the length-mismatching restrictions and providing real-time tracking of atomic-scale surface reactions, even the reaction pathway based solely on colors.

4.2. Basic Concept

In this chapter, a FP etalon was proposed to couple the gas-matter reaction to the light-matter interaction by strategically designing a platform that confines selective gas adsorption and subsequent water-forming reactions in various chemical pathways. In a thorough understanding of the underlying principle of colorimetric changes in FP etalon devices, different gas-reactive pathways at the interface between a gas-permeable polymer film and palladium (Pd) metal were observed with drastic color variation. Two distinct trends of color variations (i.e. color foggy effect vs. white-out effect) in response to the predominating gas exposure were found because of the different behaviors of water-forming reactions (water bubble formation under O_2-dominated Pd surface and water film formation under H_2-dominated Pd surfaces) (Figs. 4.1 and 4.2). Based on knowledge of surface chemistry and sequential exotic optical phenomena by FP etalons, this chapter reports the most advanced and

practical approach for gas stimulus-induced dynamic optical coloration technology and investigated the underlying gas-matter physical/chemical interaction behaviors using simple spectroscopy and naked-eye monitoring methods. Based on this structure, atomic-scale surface reactions were verified beyond the optical diffraction limit. Furthermore, this approach can fabricate scalable hydrogen gas sensors. The proposed platform is fundamental for understanding basic science and the fabrication of cost-effective gas sensors for industrial applications.

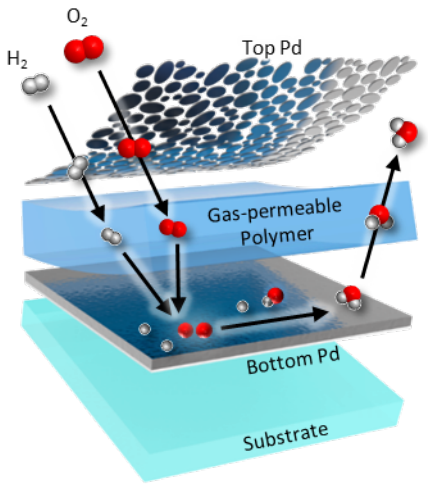

Figure 4.1: Overall mechanism and phenomena of water-forming reaction at FP etalon. Layer description of FP etalon and H_2/O_2 adsorption on the Pd surface undergoing the atomic-level catalytic reaction.

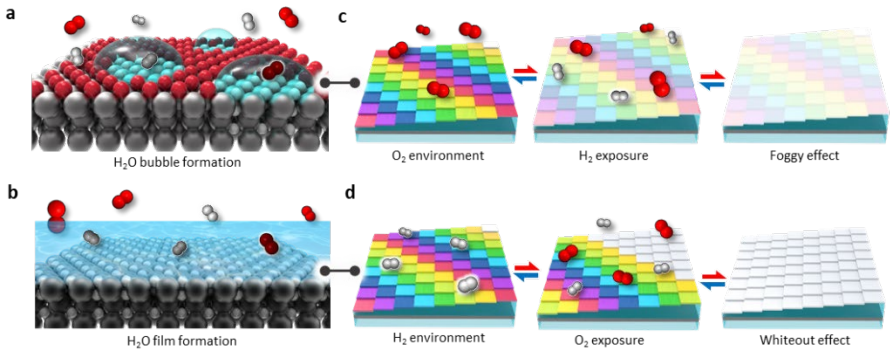

Figure 4.2: Conceptual illustrations of atomical gas adsorption and sequential water-forming reactions inducing water bubble formation over the O_2-precovered (a) and H_2-precovered Pd surface (b) in response to H_2/O_2 gases exposure, resulting in optical foggy effect (c) and optical whiteout effect (d), respectively.

4.3. Experiments

4.3.1. Fabrication of Pd-based FP Etalon Substrates

On a Si wafer, 10 nm of Ti adhesion layer and 10 nm Pd layer was subsequently deposited using a thermal evaporator (MHS-1800, Muhan; 10-7 Torr; 2.0 Å/s). The PBVE polymer mixture was prepared by diluting 9.0 wt.% PBVE polymer (Chromis Technologies) in a fluoro-solvent (FC-43, Chromis Technologies) to obtain 6.0 wt.%, and then spin-coated on the Pd surface at 900 rpm for 30 s. To eliminate air bubbles inside the mixture, it was placed at room temperature for 1 h and baked on a hotplate at 50 °C, 80 °C, 180 °C for 1 h each in order, resulting in a 590 nm thick PBVE layer. The polymer layer was delicately etched using RIE (RIE 80 plus, Oxford Instrument) to modify thicknesses for different colors. Prior to top Pd deposition, a high surface energy of the PBVE film was relieved by annealing it at 180 °C for 30 min. Then, 10 nm of top Pd was thermally deposited on the PBVE film.

4.3.2. FLIC Pattern Analysis and Thickness Simulation

To uniformly cover the PBVE with a thin calcein layer, O_2 plasma surface treatment (CUTE, Femto Science) was applied to enhance surface energy. Then, 0.64 mM of calcein dissolved in dimethyl sulfoxide(Sigma-Aldrich) was spin-coated on the PBVE surface at 4500 rpm for 60s, followed by N_2 blow drying. While 10 % of H_2 in N_2 carrier gas was supplied to the gas chamber, the fringe patterns on the sample surface were monitored with a microscope using

fluorescein isothiocyanate (FITC) filters. Fluorescence intensity profiles were measured to examine water bubble height.

For the 3D analysis of water bubbles, calcein, as the fluorescent dye with excitation (λ_{ex}) and emission (λ_{em}) wavelengths of 488 and 525 nm, respectively, were applied on top of the PBVE layer. Because the z-direction height of the calcein layer (z) varies owing to the water formed underneath it, the normalized fluorescence (FL) intensity (F) can be derived using the following equation:

$$F = sin^2\left(\frac{2\pi(n_{\text{water}} \cdot z + n_{\text{PBVE}} \cdot t_{\text{PBVE}})}{\lambda_{\text{ex}}}\right) sin^2\left(\frac{2\pi(n_{\text{water}} \cdot z + n_{\text{PBVE}} \cdot t_{\text{PBVE}})}{\lambda_{\text{em}}}\right) \quad (4.1)$$

where t_{PBVE} is the thickness of the PBVE, and both the refractive indices of water (n_{water}) and PBVE (n_{PBVE}) were approximated to be 1.34. As the height (h_{water}) and radius (r) of the water bubble are determined, the corresponding z-coordinate at the x-position can be calculated as follows:

$$z = \frac{h_{\text{water}} + t_{\text{PBVE}}}{r}\sqrt{r^2 - x^2} \quad (4.2)$$

derived from an elliptical equation. For example, when t_{PBVE} is 180 nm, the number of interference patterns increases for every 110 nm increment of h_{water} from 110 to 550 nm, as shown in Fig. 4.3. Therefore, it briefly interprets the 3D shape of the water bubbles.

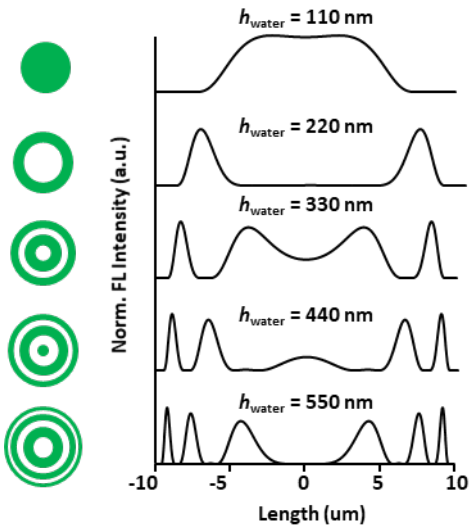

Figure 4.3: Expected interference patterns and FL intensity depending on the water bubble height. Simulated normalized FL intensity for h_{water} from 110 nm to 550 nm when t_{PBVE} is 180 nm.

4.3.3. Gas Control and Optical Analysis

To control the H_2 concentration, a mass flow controller (MFC) was used for each gas. To realize the atmospheric conditions, a 1:4 ratio of O_2 and N_2 was maintained for the carrier gas. The experimental setup is shown in Fig. 4.4. The outlet of the chamber was connected to a hydrogen concentration analyzer (EN-600, Shanghai ENCEL Instrument Co., Ltd.) to monitor the real-time H_2 concentration inside the chamber. The reflectance spectrum was measured using ultraviolet-visible spectroscopy (USB4000-UV-VIS, Ocean Optics) with normal incident white light (DH-MINI, Ocean Optics) and a reflection probe (R400-7-SR, Ocean Optics).

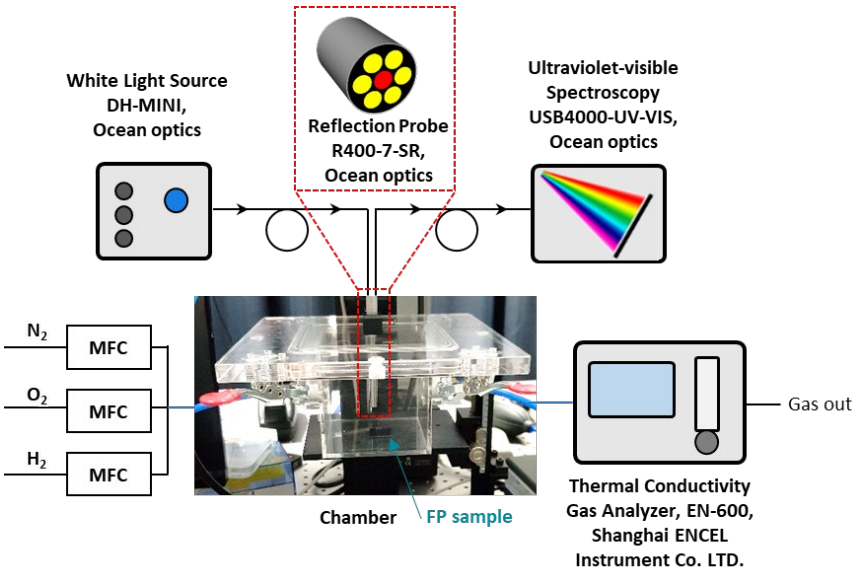

Figure 4.4: Experimental Set-up. Schematic diagram of the gas exposure chamber with reflectance spectrum measurement. Each gas flow rate of N_2, O_2, and H_2 is precisely controlled by a mass flow controller (MFC), and the H_2 concentration of the outlet gas was continuously monitored.

4.3.4. DFT Calculation

All DFT calculations were performed using VASP6 (Vienna Ab-initio Software Package) with the projector augmented wave method (PAW) [65-68]. The plane wave kinetic energy cutoff was set at 520 eV and Monkhorst-Pack 3×3×1 points were used for calculations [69]. Perdue-Burke-Ernzerhof (PBE) exchange-correlation functionals were used [70]. The forces acting on each atom were relaxed to under 0.02 eV/Å.

Four metallic layers of the face-centered cubic (FCC) Pd(111)-p(2×2) and PdH(111)-c(2×2) surfaces were chosen to calculate the initial water formation reaction steps. The two bottom layers were fixed to the bulk coordinates. An oxygen coverage of 0.50 monolayer (ML) and hydrogen coverage of 0.50 ML were set to model the initially oxygen-saturated Pd and hydrogen-saturated PdH surfaces.

4.4. Results and Discussions

4.4.1. Interfacial Confinement of Water-forming Reaction at FP Cavity for Dynamic Plasmonic Coloration

The FP resonance cavity, in which a gas-permeable polymer is sandwiched between the top and bottom Pd metals, was prepared to improve the performance of the gas-induced plasmonic coloration. Only H_2 and O_2 penetrate and reach the polymer/bottom Pd interface where a catalytic reaction is expected. According to the pertinent literature, the dissociative adsorption of H_2 and O_2 occurs competitively on the Pd surface, forming H_2O [71-73]. Based on DFT calculations, exothermic steps for H_2O generation with different energy pathways are expected as a function of the surface chemistry of the Pd(111) surface (O- vs. H-covered Pd). The H-covered Pd surface shows preferred H_2 dissociation over the O-covered Pd surface due to the exothermic transition from state II to III (Fig. 4.5). This led us to assume that different ratios or types of H_2O genesis are expected. For instance, the different H_2O genesis pathways and resultant distinct H_2O types (i.e. bubbles and film) may cause distinct optical phenomena (optical foggy effect and white-out effect). Then, we can monitor the atomic scales of surface catalytic reactions in color via light-matter interactions. Consequently, real-time and dramatic color changes in response to the alteration of the physical properties of the dielectrics (polymer insulating layer and newly formed water film) of the FP etalon can be realized by coupling the light-matter interaction of the FP cavity with the gas-matter reaction, which

permits the water droplets/film and concomitant structural color change through gasochromic observation.

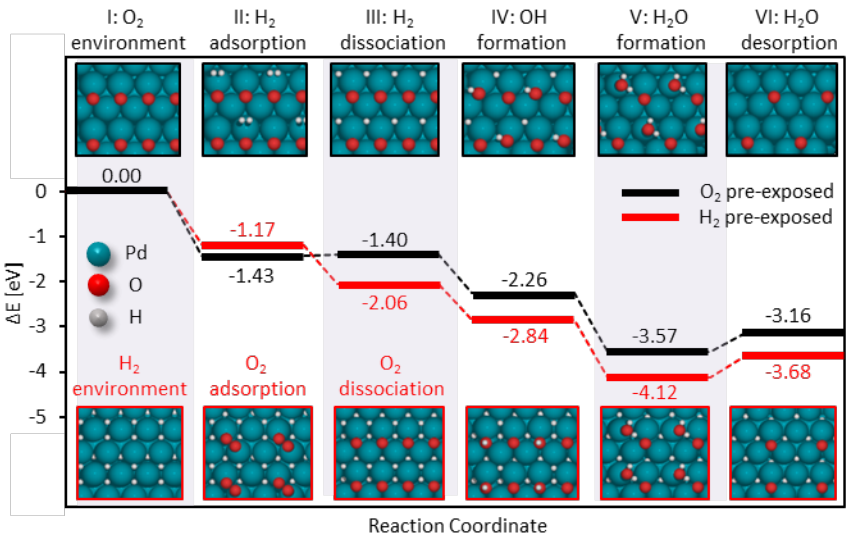

Figure 4.5: Energy profiles for dissociative adsorption of H_2/O_2 and H_2O formation/desorption on the Pd(111) surface initially exposed to O_2 (Black) and H_2 (Red)

4.4.2. Water Bubble Formation at the Polymer/Pd Interface

Figure 4.6 shows the Pd-assisted catalytic reaction that produces water bubbles. At equilibrium, as the physisorption of O_2 on the Pd surface is thermodynamically more favorable than that of H_2, the surface coverage of adsorbed H_2 is relatively small [74]. High surface coverage of O_2 on the Pd surface interferes with the dissociative adsorption of H_2 involved with the correlation between the d-orbital of Pd and the s-orbital of H, degrading the efficiency of the water-forming reaction. When the coverage of dissociated H_2 on the Pd surface exceeds the threshold, spontaneous genesis of water film ($O_2 + 2H_2 = 2H_2O$) occurs at room temperature, experimentally proven under the critical pressure ratio of $O_2/H_2 < 2.5$ [71]. However, for spatially H_2-covered spots surrounded by overwhelming O_2-covered area, the water-forming reaction will occur in the forms of 'water bubbles' discarding the possible scenarios of a nanometer-thick water film and their successive growths via coalescence processes. In addition, the H_2O evaporation rate should be suppressed and minimized than the H_2O generation rate to maintain the pre-formed H_2O bubbles. For this, the Pd surface was coated with a 180-nm thick PBVE film as a sieve layer with selective gas permeability only for O_2 and H_2 [75]. Oxygen permeability through a Pd-covering PBVE membrane is essential to trigger the water-forming reaction. As a control experiment, we compared the gas colorimetric behavior of another sample prepared using O_2-impermeable polymethyl methacrylate (PMMA) as a dielectric film. There

were no water bubbles under identical H_2 conditions, confirming the role of dielectric films in water formation via selective gas permeability (Fig. 4.7).

To investigate the formation of water bubbles by H_2 adsorption at the PBVE/Pd interface, a sample with PBVE/Pd/titanium (Ti) (180 nm/10 nm/10 nm) on a silicon (Si) substrate was exposed to 10% H_2 in a gas chamber (N_2:O_2 = 4:1 as a carrier gas), and the dynamic water bubbles formation was monitored in real-time under a microscope (Fig. 4.8). A Ti layer promoted adhesion between the PBVE and Pd films and suppress abrupt phase change (from α to β phase) causing Pd film deformation such as peeling and wrinkles [76]. Randomly positioned outbreaks and growth of micron H_2O bubbles, followed by coalescence between neighboring bubbles, were observed (<130 s), which varies from previous studies of nanometer-thick transient water generation without a Pd-covering membrane [72, 73, 77]. After turning the H_2 supply off (>130 s), we observed a gradual decrease in the water bubble volume and subsequent disappearance (225 s) equal to the initial state (0 s).

Three-dimensional (3D) PBVE deformation during the water-forming reaction was confirmed via fluorescence interference contrast microscopy (FLIC) [78]. For FL visualization, a thin layer of calcein as the fluorescent dye was coated atop the PBVE surface, followed by 10% H_2 exposure (Fig. 4.9). Interference-assisted alternative bright/dark patterns arise from the vertical movement of the dyes, and FITC-labelled calcein and the resultant fringe patterns allow an analysis of the height of water bubbles (Fig. 4.9b). Figure 4.9c shows the normalized FL intensities measured from Fig. 4.9b as a function of the water-bubble scanning length with corresponding simulation results. The

intensity profiles of the fringe patterns along the dashed lines confirm that more fringes can be created as the exposure time or H_2 concentration increases. Tracking FL molecules via simulations revealed that the PBVE membrane swelling owing to the water bubble growth underneath the calcein layer experienced a height alteration of 138 nm (red), 290 nm (blue), and 470 nm (orange) during 100 s (Figs. 4.9d).

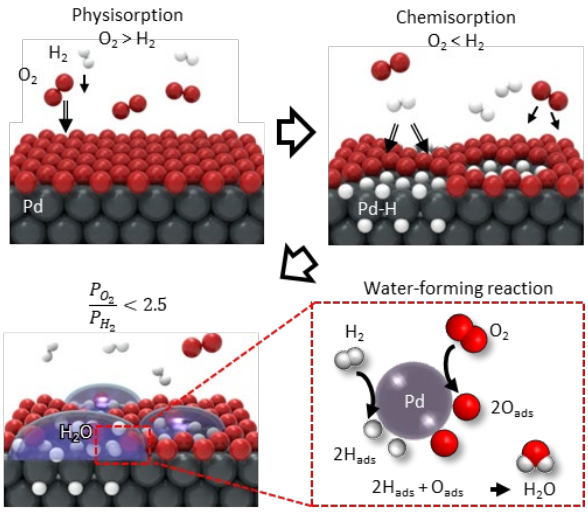

Figure 4.6: Schematic illustrations for understanding the underlying mechanism of water bubble formation on Pd surfaces after H_2/O_2 adsorption undergoing the atomic-level catalytic reaction.

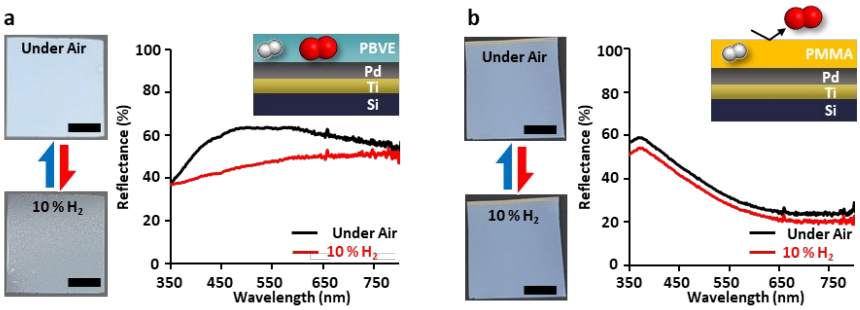

Figure 4.7: Effect of gas permeability of the insulator on water-forming reaction and following spectral response. Photographs and measured reflectance spectrum of the Pd/Ti/Si sample coated with 180 nm of PBVE (a) and PMMA (b) under air (top, black) and 10% H_2 exposure (bottom, red). Scale bars, 5mm.

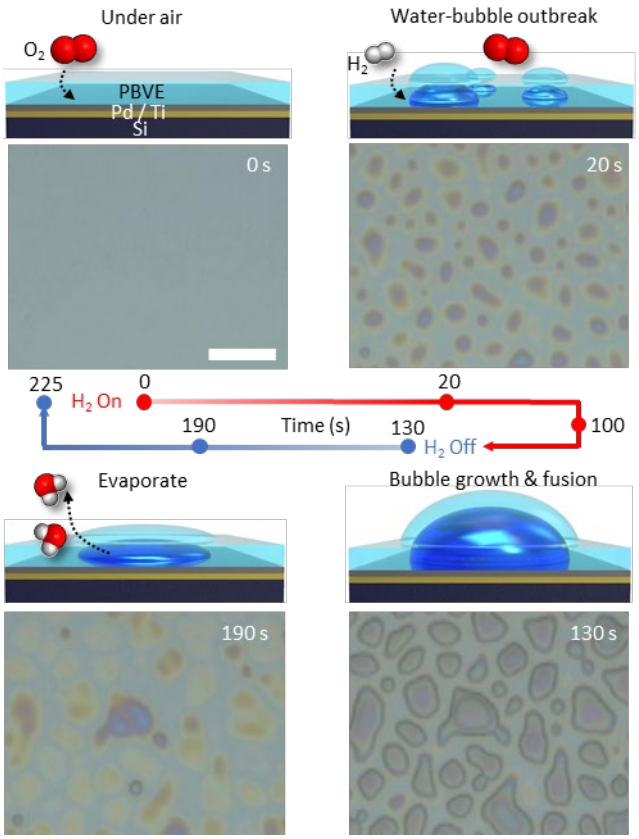

Figure 4.8: Top-view microscopic images and corresponding side-view illustrations of PBVE-coated Pd surface under H_2 gas exposure at atmospheric condition. Scale bar, 10 μm.

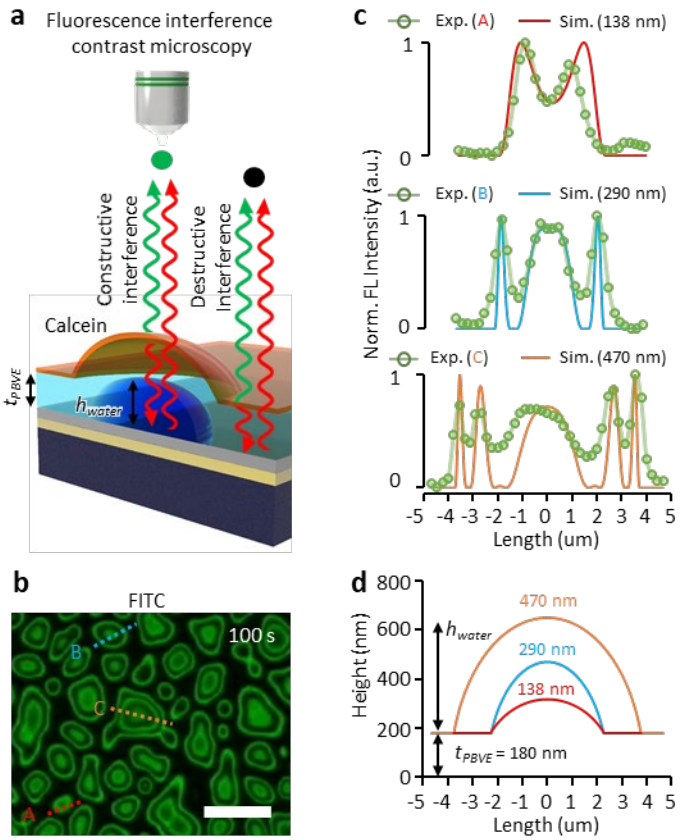

Figure 4.9: Concepts and working principles of FLIC observation for micron water bubble formation at PBVE/Pd interface. d) FL intensity of micrograph monitored using FITC filter (100 s). e) Measured FL intensities from dashed lines of (d) (A: red, B: sky-blue, and C: orange) with simulated FL curves (solid-lines) with respect to the h_{water} modulations. f) FL intensity-based simulation results of PBVE deformation by water bubble formation. Scale bar, 10 μm.

4.4.3. Optical Foggy Effect by Water Bubbles Induced Light Diffusion

This study realizes various color changes by reinforcing light-matter interactions based on the volume change of the dielectric layer. To boost the light-matter interaction, the FP resonator [79], underpinning the naked-eye observation of the water-forming reaction, was adopted by depositing another Pd layer on the PBVE surface. A MDM structure, known as the FP etalon, enables sensitive color variations as a function of physicochemical properties, such as the thickness and RI of the dielectric layer [35, 51, 54, 80]. Thus, their modulation induced by water bubble formation and growth at the PBVE/Pd interface would cause a dramatic color shift. In addition, hemispheric water bubbles may cause diffuse reflection of incident light as they act as individual lenses (Fig. 4.10).

Designing a perforated top metal layer with efficient transreflective characteristics is essential for generating the FP resonating effect. The optimum deposition thickness of 15 nm with a volumetric filling fraction of 0.45 for the nanoparticulated Pd layer was selected through experimental optimizations and a computational simulation to advance the FP resonance effect for producing wider range of color displays. The top-view (Fig. 4.10b) and side-view (Fig. 4.10c) SEM images show that a 15-nm-thick Pd layer was deposited on the PBVE film. The FP etalons on a 4-inch Si wafer with varying dielectric PBVE thickness, t_{PBVE}, values from 0 nm to 590 nm at 10 nm intervals were controlled

by a delicate plasma etching process, showing excellent correspondence in reflection color trends with simulation results (Figs. 4.10d and 4.11). The t_{PBVE} increases from the left-bottom corner (0 nm) to the upper-right corner (590 nm). Figure 4.11 shows that reflection colors of the FP etalon turn discolored and eventually become foggy when exposed to 10% H_2 under atmospheric conditions. As predicted in Fig. 4.10, diffuse reflection due to newly formed micron-water bubbles interrupts the FP resonance, thus resulting in foggy colors (bottom-right photograph of Fig. 4.11, at 6 min), and this transition is fully reversible. After establishing that color transition occurs due to water bubble formation in the dielectric layer, we quantified the critical gas values that trigger color transitions. The reflectance spectra at the center yellow area (red-dashed square in Fig. 4.11) were measured as H_2 concentration was gradually increased and decreased by 1% every 5 min (Fig. 4.12a). When H_2 concentration reaches 7%, nearly corresponding to the critical ratio of O_2/H_2 = 2.5, the waveform of reflectance over the visible range begins to flatten (lowering peaks and raising dips shown in Fig. 4.12b). By plotting the peak reflectance around 400 nm wavelength depending on H_2 concentration (Fig. 4.12c), the water-forming reaction vigorously occurred from 7% to 8% and then decreased from 4 %. The rapid reduction in the peak reflectance over 7% H_2 indicates that the water bubble formation and coalescence are instantaneously accelerated at around a critical ratio of 2.5. The slow recovery of the peak reflectance with decreasing H_2 concentration is probably attributed to the thermodynamically unfavorable desorption of H_2O molecules at the Pd surface (endothermic transition from state V to VI in Fig. 4.5). At 4% H_2, the recovery

rate gradually increased because minuscule water bubbles only existed. An H_2 concentration-dependent change in the peak reflectance (lowering peaks and raising dips) was continuously observed in multiple H_2 injection/purging cycles, demonstrating the excellent repeatability ($\geq$28×) of our FP etalon, considering that typical metal-hydride-assisted color displays showed limited ($\leq$20×) operating cycling numbers (Fig. 4.13) [14].

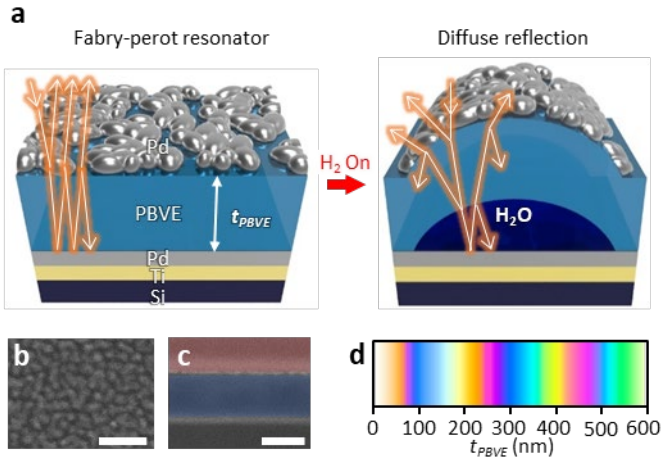

Figure 4.10: Schematic illustrations of FP etalon prior to (left) and post to (right) the water bubble formation with resultant optical effect. b, c) SEM images of the etalon sample. Top-view- (b) and pseudo-colored side view images (c) after focused ion beam milling (red: epoxy coating layer, blue: PBVE). d) Simulated reflection color gradient on the FP etalon with different thicknesses of the PBVE, t_{PBVE}. Scale bar in (b), 50 nm. Scale bar in (c), 200 nm.

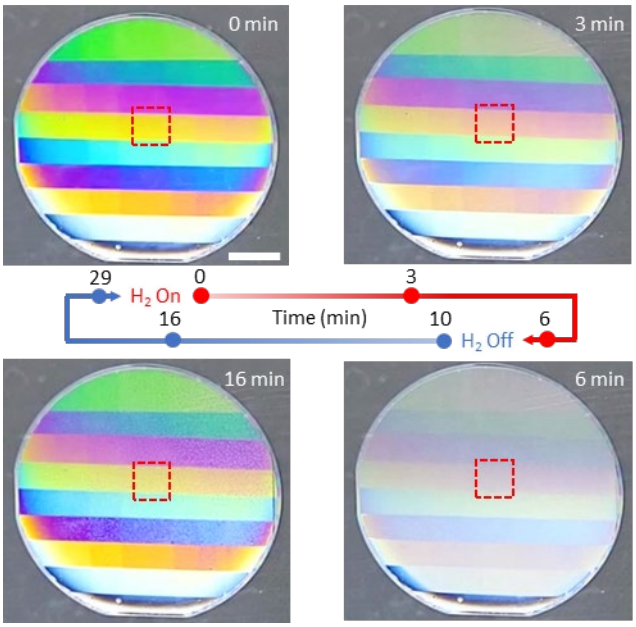

Figure 4.11: Photographs of FP etalon on a 4-inch wafer under 10% H_2 showing color reversibility at atmospheric condition. Scale bar in, 2 cm.

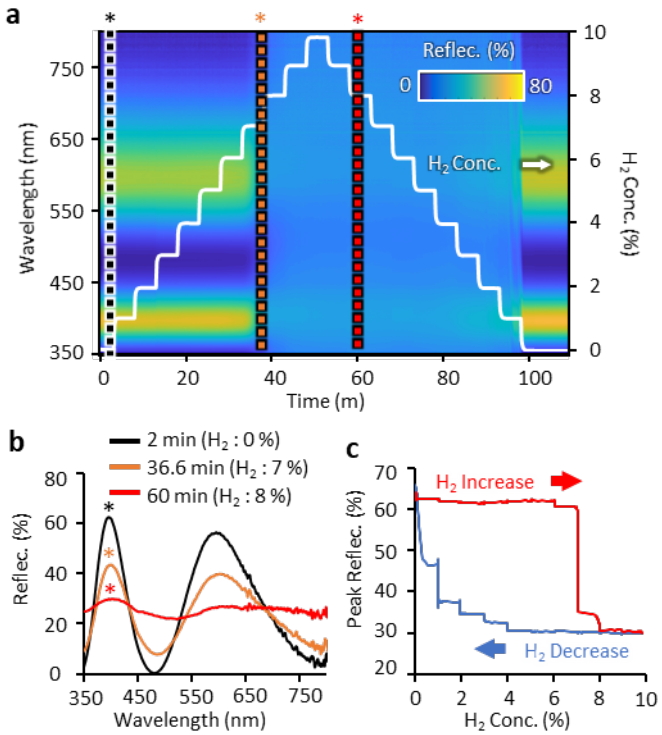

Figure 4.12: (a) Measured reflection spectra as a function of H_2 concentrations (0-10%) at the red-dashed area of Fig. 4.10. b) Sampled reflection spectra (each color matches to dashed lines in (a)). c) Alteration of an amplitude of reflectance peak while varying H_2 concentration.

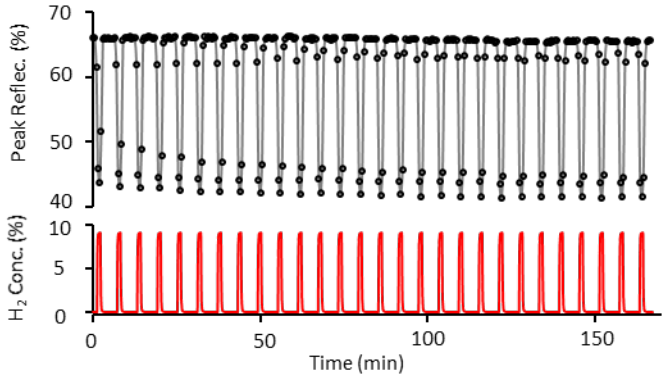

Figure 4.13: Repeatability test of FP etalon undergoing H_2 exposure for 28 times over 2.5 h.

4.4.4. Multichromatic Change by the Water-film Formation and Following Whiteout Effect

O_2-predominated Pd surface promotes random water bubble formation under H_2 gas exposure. The Pd-dominated gas can determine the surface chemistry and resultant water formation types. The colorimetric changes in the FP etalon after preparing the H_2-predominated Pd surface before the O_2 gas supply was investigated and it was examined whether such different surface properties promote distinct forms of water products. In accordance with previous studies that a nanoscale water film could be formed when a Pd surface is entirely preoccupied with H_2 before the O_2 gas supply [73], the FP etalon was exposed to 10% H_2 for 5 min to induce full β-phase Pd hydride (PdH) and H_2-predominated Pd surface [81], followed by 20% O_2 gas supply (Fig. 4.14). The uniform formation of nano-water film at the PBVE/Pd interface is useful in the optical interpretation since the RI of water (n = 1.33-1.34 in the visible range) is similar to that of PBVE (n =1.34 at 550 nm and 1.333 at 1.55 um). Thus, generating a nanoscale water film underneath the PBVE layer can be simply interpreted as thickening the dielectric layer of the FP etalon, enabling multichromatic changes as a function of the water film thickness. Figure 4.15 shows reversible and drastic color changes in the 10% H_2 pre-exposed etalon under 20% O_2 gas exposure. Compared with the color changes above (Fig. 4.11), a rapid and dramatic color change was observed, producing an exotic optical

white-out effect in 10 min. In addition, reversible color recovery was completed within 20 min after cutting off the O_2 supply.

To elucidate the water-film thickness-based color variation on the FP etalon, the time-lapse spectra was analyzed at the center yellow area (red-dashed squares in Fig. 4.15) with increasing O_2 concentrations up to 20% by 2% every 1 min (Fig. 4.16). The red shift of the measured waveform was initiated at 12% O_2 concentration (8 min) and maximum before the gas cut-off (12 min). The red shift in the visible range is attributed to the increased effective thickness of the dielectric film (PBVE + water). A simulation was conducted by varying $t_{\text{dielectric}}$ to confirm the effect of dielectric film thickening on the color shift of the FP etalon. Simulations verified that the measured spectral shifts arose from the dielectric thickening effect, that is, additional H_2O film formation below the PBVE layer. The second resonance peaks, extracted from the reflection spectra (Fig. 4.16a), show not only a red shift but also an overall decrease in magnitude (Fig. 4.16b). From an optical analysis perspective, the thickening of the dielectric film caused the coexistence of a higher-order resonance wavelength in the visible range, resulting in the white-out of the FP etalon (Fig. 4.16c).

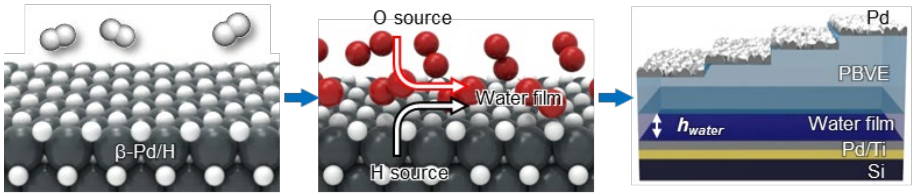

Figure 4.14: Schematic illustrations describing water-film formation on β-phase PdH surface.

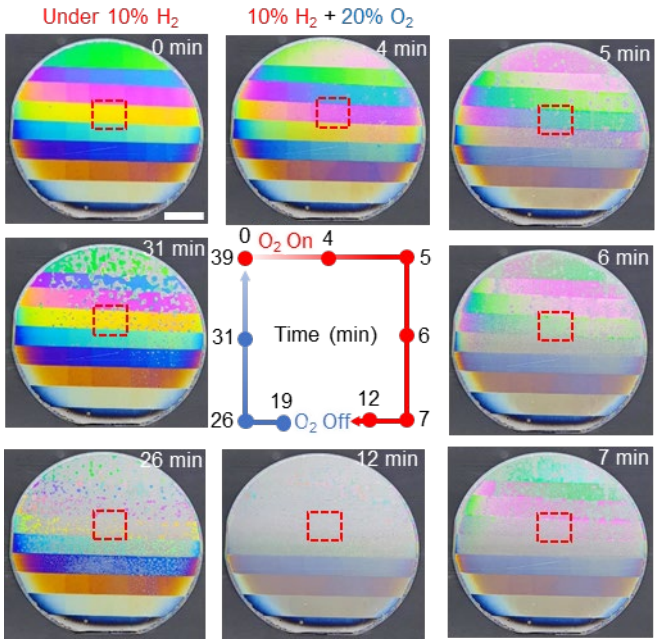

Figure 4.15: Time-lapse photographs of the FP etalon under 10% H_2 followed by 20% O_2 exposure. Scale bar, 2 cm.

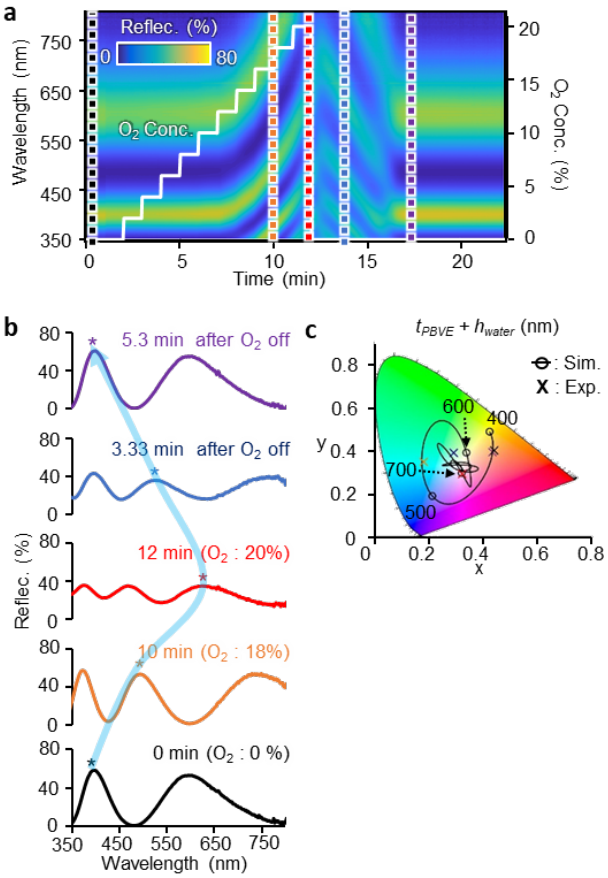

Figure 4.16: (a) Measured reflection spectra as a function of O_2 concentrations (0-20%) at β-phase PdH surface (red-dashed area of Fig. 4.15). (b) Sampled reflection spectra (each color matches to dashed lines in (a)). (c) Simulated colors of the FP etalon depending on t_{BPVE} (400-1200 anm) plotted on CIE 1931 color space (black). The measured spectra from (b) are plotted with respective colors.

4.4.5. Scalable and Transparent Display for Gas Detector via Water-forming Reaction

Implementing the water-forming reaction at the gas-permeable polymeric membrane and Pd interface can cause substantial innovations in various hydrogen applications. Forthcoming commercial coloration device technology must fulfil both aesthetic elements and outstanding performance and must be prepared in a facile fabrication process over various solid supports (such as a transparent and flexible substrate) in a scalable manner. Furthermore, it would be beneficial if the MDM could comprise various dielectric and metal components with identical functions. Respectively, our proposed technology can realize various theme colors by simply controlling the thickness of the metal and polymer layers. Furthermore, delicate and aesthetic drawings or patterns of a few microns can be easily fabricated via compatible semiconductor processes, meeting demanding industrial needs with high prospects for commercialization and technological standardization.

By depositing all metal layers through a shadow mask, a flower-patterned etalon (f-etalon) was prepared on a 2.5 cm × 2.5 cm glass substrate (Fig. 4.17). Because $t_{\text{dielectric}}$ determines the overall reflection colors, spatially selective PBVE etching by the RIE process produces a wide color range of flower patterns. The top Pd, as a trans-reflective layer, can be replaced by other perforated metal films, including Au or silver (Ag), as they maintain color changes in response to the gases (Fig. 4.18). No colorimetric changes were

monitored when top metal metals were passivated with a flat film without nano-punctuation. Fast deposition rate (1 Å/s) results in full coverage of the dielectric layer barely allowing nano-apertures formation at the top metal layer when compared to the slow deposition rate (0.2 Å/s) of f-etalon. The f-etalons prepared by Au and Ag top metals showed drastic color changes under H_2 exposure.

For accomplishing water-forming-assisted color changes, a perforated top metal film is essential because the opening at the top metal layers allows gas to penetrate across the top metal layer. Figure 4.19 represents that the 'optical foggy effect' (upper line) and 'white-out effect' (bottom line) were still available in the f-etalon having10-nm-thick Ag top metal, compared with the same color-changing behavior at the f-etalon with 10-nm-thick top Pd. For instance, the reference color of the f-etalon (red square of yellowish flower petals) gradually faded and then shrouded by a pale gray color at 600 s (foggy effect). Meanwhile, the yellow color of the identical zone turned white within 240 s (white-out effect) after O_2 injection.

Structural color intrinsically produces angle-dependent color variation due to its increased optical path length in the resonating dielectric film. The etalon color varied with increasing viewing angle (from 0° to 75°), resembling the effect of thickening the optical cavity. Because the diffuse reflection by water bubbles is angle-independent, the foggy effect can occur at any viewing angle (Fig. 4.20), making the proposed etalon structure applicable to gas leakage warning smart windows. As schematically demonstrated in Fig. 4.21a, the f-etalons installed in a hydrogen gas storage facility can instinctively recognize

the leakage of H_2 gas by dimming the original colors of the flower patterns. This scenario was demonstrated using an actual miniature model by placing four f-etalon samples inside a miniature gas tank storage room (Fig. 4.21b).

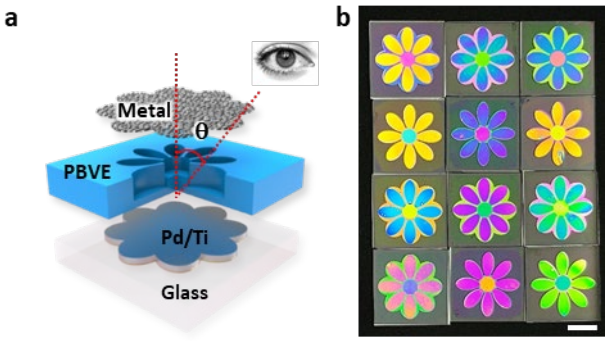

Figure 4.17: Schematic layer description (a) and photograph (b) of 12 fabricated f-etalon samples on glass substrate. Scale bar, 1 cm.

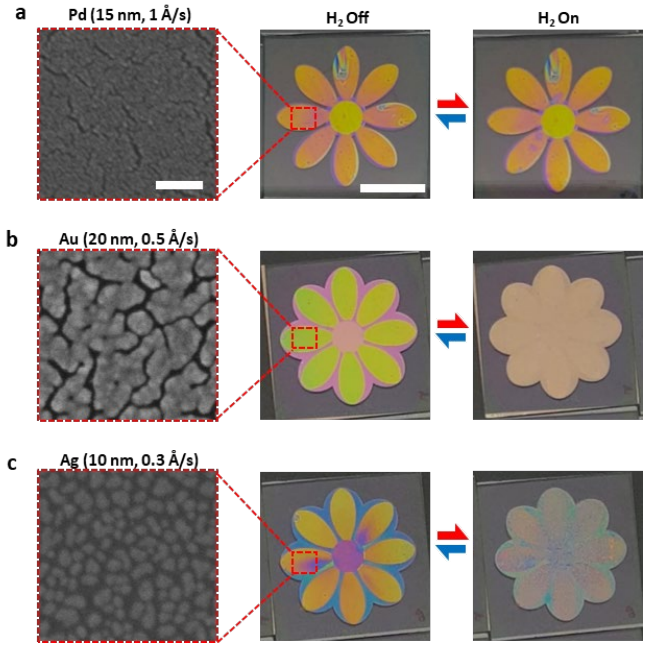

Figure 4.18: The f-etalons prepared with different top metals with various filling fraction. Top view SEM images and photographs of f-etalons of which top metals are a film-like Pd (a), nanoparticulated Au (b), and nanoparticulated Ag (c). For water-forming test, identical gas moods were exposed to the samples. Scale bars in (a), 100 nm (left), and 1 cm (middle); the scale bars in (a) also applies to (b) and (c).

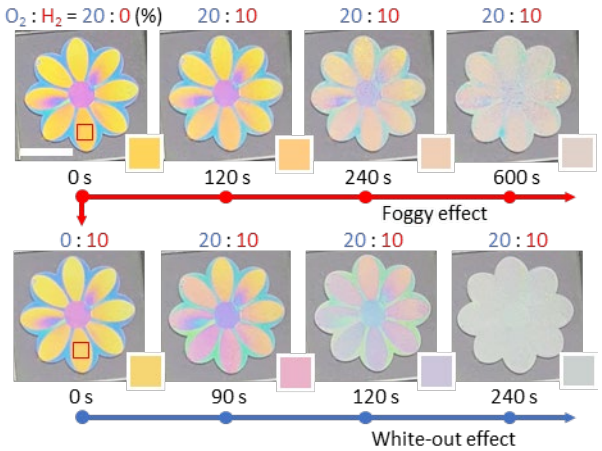

Figure 4.19: Photographs of the sample with Ag top film displaying color variation in response to different gas composition. Scale bar, 1 cm.

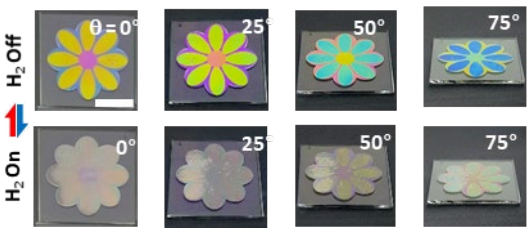

Figure 4.20: Angle-dependent color variation and foggy effect under H_2 exposure. Scale bar, 1 cm.

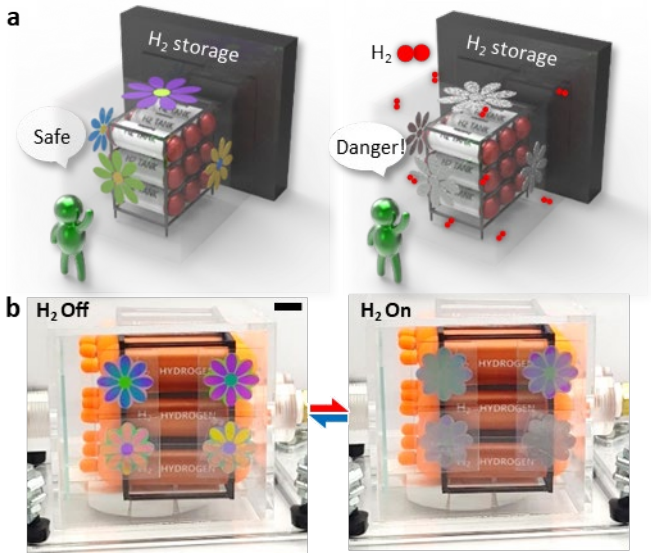

Figure 4.21: Scheme of f-etalon on glass applied for H_2 leakage warning window (a) and its demonstration in a miniaturized H_2 storage facility (b). Scale bar, 1 cm.

4.5. Summary

Water-forming reactions and O_2 species in the air have been considered as interrupting side reactions and impurities to avoid H_2 storage and sensing technologies [82]. Here, these unwanted phenomena were applied to make the molecular reaction of H_2 and O_2 visible by transducing the gas-matter reaction into light-matter interactions over the Pd catalyst. In the transducing process, the formation of an H_2O film at the PBVE/Pd interface is critical in dynamic coloration as it determines the overall $t_{dielectric}$ constant.

The strategic passivation of deformable PBVE films over bottom Pd metals allows H_2O products to accumulate at the microscopic level via successive growth or coalescence processes. The selection of a gas-permeable polymer membrane as a dielectric film plays multifunctional roles: i) a physical barrier for the suppression of H_2O evaporation once they are generated at the PBVE/Pd interface, ii) a dielectric layer allowing transmission of the incident light, and iii) reliable detection performance even in a humid environment which is one of the chronic hurdles of electrically biased H_2 sensors [83]. Applying a perforated top metal film is essential for creating structural colors by its efficient transreflective characteristic yielding the FP resonating effect and for allowing gas penetration through the nano-apertures of the metal film. There was no color change under H_2/O_2 exposure when the top Pd was nanohole-less, which confirms that the perforated metal film is key for dynamic coloration, as it allows gas reactants and products to cross the metal film.

Leveraging the underlying principle of the FP resonator, the in-situ tracking of different types of H_2O products was optically realized via gas

stimulus-induced dynamic optical coloration. Based on the color variation as a function of dielectric changes, the experiments showed exotic optical phenomena: the water bubble-assisted ‘optical foggy effect’ and the water film-assisted ‘optical whiteout effect’. Quantitative analysis of H_2O production/desorption has been achieved only by mass spectrometry [84]. But no further information has been provided, such as tracking chemical reaction pathways. The proposed dynamic optical coloration technology provides information on how H_2 and O_2 react at the PBVE/Pd interface and allows the tracking of gas-matter physical/chemical interaction behaviors using simple spectroscopy and naked-eye monitoring methods.

Chapter 5. Fabry-Perot Cavity Control for Tunable Raman Scattering

5.1. Introduction

Recently, a promising future analytic approach that enhances the conventional SERS platform with fixed limit of detection (LoD) values or static optical performance as an analytical device has been proposed not only to lower the LoD but also to provide additional functionality to Raman-based platforms. New trends in the exploration of "dynamic Raman scattering technology" demonstrate their flexible optical performance for maximizing the SERS signals in response to the various analytes, excitation lasers, and surrounding environments by modulating composing materials, shape, periodicity, working media during measurements. For this purpose, an EM near-field enhancement at local areas around metal nanostructures and its far-field response should be considered as they govern the overall performance of the SERS techniques, that is, SERS EF. The near-field enhancement by a localized EM field has contributed to an improved understanding of the molecular interactions [85] and inter-particular distance [39], while the far-field optical response has enabled the experimental tracking of the inter-spatial and geometrical properties of the constituting Raman structures. A change in such inter-molecular [86] or inter-particular spacing modifies both the near-field and far-field enhancements, thereby tuning the overall optical absorption in response to pH [86], temperature [87], strain [88, 89], moisture [90, 91], biochemical

molecules [92], and gases [93]. The SERS effect is highly dependent on the composition of materials and their nanostructured alignment/arrangement, and the development of a SERS platform that is reliable and reproducible in response to repeatable external stimuli-driven chemical/geometrical deformation remains a technical hurdle for practical applications. For example, highly populated nanoparticulate SERS chips may lose their Raman sensitivity owing to the reduced near-field SERS effect during the modulation of the interparticular spacing for far-field response modification [87]. Therefore, it is desirable to sustain the optimal near-field enhancing structure while modulating the far-field response.

5.2. Basic Concept

In this chapter, placing a mirror metal underneath the near-field-generating optical hotspots with a controlled vertical gap distance, as well as engineered materials, could prevent the loss of the overall SERS effect. The design of a reconfigurable optical cavity that re-optimizes the optical interference for maximum SERS EF may tune the photonic performance of analytical devices with controlled Raman scattering. To do this, we propose the FP etalon to maximize the SERS EF values by positioning the in-plane near-field plasmonic metal nanostructure as a top film. The far-field response is tuned via physicochemical modulation of the sandwiched dielectric layer between metal films. The mechanism of the optical interference from the FP resonator is far-field in nature, thereby tuning the overall magnitude of the Raman signals determined by the physical properties of the dielectric films [94]. In an FP

etalon, the nanoparticulated top metal layer plays multi-functional roles as (i) a "liquid channel" enabling solvent permeation across the top solid film, (ii) "optical hotspots" generating the near-field SERS effect, and (iii) a "shadow mask" enabling spatial etching of underneath dielectric film. Computational and experimental analyses have been thoroughly proven not only to optimize near-field Raman enhancement but also to modulate the far-field Raman response. The featured Raman switching effect was further applied to dynamic Raman anticounterfeiting devices under solvent exposure.

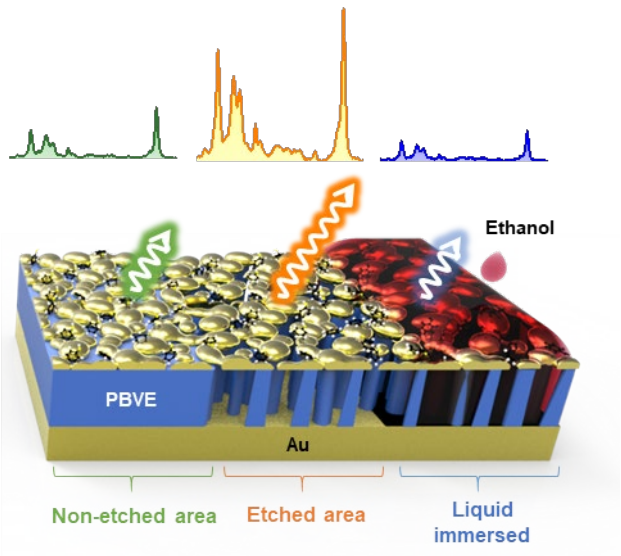

Figure 5.1: Conceptual illustrations of tunable Raman signals via the structural modulation of FP etalon.

5.3. Experiments

5.3.1. Fabrication of an FP Etalon Substrate for Dynamic SERS Signal Tuning

A 10-nm Ti adhesion layer and a 120-nm Au layer were deposited on a Si wafer using an e-beam evaporator (EI-5K, ULVAC). PBVE films having various thicknesses were spin-coated with the PBVE polymer solution [a mixture of 9.0 wt% PBVE solution (CyclAFlor Clear, Chromis Technologies) and fluoro solvent (CyclASolv-PFC180, Chromis Technologies)] and annealed on a hotplate at 80 °C for 1 h. A nanostructured top Au layer was slowly deposited on the PBVE dielectric layer via thermal evaporation (10^{-7} Torr, 0.3 Å/s). Finally, oxygen plasma reactive ion etching (RIE, 100 mTorr, O_2 gas flow of 100 sccm, and RF power of 50 W) was performed to create hollow voids in the dielectric layer.

5.3.2. SERS Measurements

To anchor thiophenol on the Au nanostructured layer, the substrates were immersed in a 1×10^{-3} M thiophenol-ethanol solution for 20 min. Subsequently, the samples were soaked in ethanol to eliminate residual analytes and were then dried. For the message-encryption sample, the substrate was placed on a thiophenol solution with the top Au layer facing downward. The Raman spectra were obtained using a confocal Raman microscope (inVia Reflex, Renishaw) with an excitation laser at a wavelength of 785 nm (laser power: 2.5 mW and laser spot size: 2 × 10 μm, ellipse) and a 50× objective lens of NA = 0.5 (Leica,

Germany). Raman signals were measured at an exposure time of 1 s. Several Raman measurement conditions were modified for specific cases. For example, Raman mapping images were obtained with an exposure time of 0.5 s, and the 1,2-bis(4-pyridyl)ethylene (BPE) Raman spectra were measured by drop-casting BPE-ethanol solutions.

5.3.3. Numerical Simulations

Finite-element method (FEM) simulations were performed using COMSOL Multiphysics 4.3a software. A 3D simulation was performed to obtain the plasmonic electric field of the nanostructured top Au film using a boundary line extracted from the SEM images. The excitation light was set to a wavelength of 785 nm and was linearly polarized. The cavity EF was calculated from a 2D MDM structure. The refractive indices of the top Au layer and the PBVE dielectric layer were estimated using BEMT. In the simulation, 750–950 nm wavelength light was used to consider the electric field of the excitation and scattering light. The maximum electric-field intensity was extracted from the top Au layer, and the cavity EF was calculated using Eq. (1.1).

5.4. Results and Discussions

5.4.1. Underlying Principles of Tunable SERS Effect on the FP Etalon

Figure 5.2 illustrates the SERS effect of the FP etalon and randomly dispersed self-assembled Au nanoparticles over the hydrophobic polymer, PBVE. First, a 120-nm-thick Au film was deposited on the Si surface, followed by a 240-nm-thick PBVE coating via a spin-coating process. PBVE was chosen as the dielectric film because of its low surface energy for low-density Au nucleation and its excellent transparency (>95%) in the visible spectrum. Then, using a single thermal deposition step with a slow evaporation rate (0.3 Å/s), a uniform and large-area Au film having nanonetworks with nanoapertures was prepared [35]. Given that the analytes spreading over a flat Au film barely yield Raman signals, our single-step technique for forming a porous Au film via a conventional thermal evaporator is highly advantageous not only in its simple, scalable, and cost-effective process but in generating strong near-field Raman enhancement by abundant nanogaps in the networked film.

The far-field Raman enhancement induced by optical interference can be combined with the near-field enhancement in a simple multiplicative manner [95]. For the far-field modulation of the Raman enhancement effect, which determines the overall SERS EFs through the optical interference of the FP etalon, its physical parameters should be considered. It is widely known that the FP cavity generates far-field resonance through the underlying principle of optical interference; therefore, geometrical or material modulations of the

dielectric film (*e.g.*, thickness and RI) lead to the manipulation of optical resonances. As conceptually described in the right schematics of Fig. 5.1, a combination of a near-field-enhancing nanogap-rich porous metal layer (Fig. 5.3a) and an FP cavity with tunable dielectric layers (Fig. 5.3b) obtained by accessing external air or liquids will provide an opportunity to dynamically manipulate the overall SERS EFs. For example, when the resonance wavelength, λ_{res}, of the FP etalon is mismatched with the wavelength of excitation, a weak SERS signal can be detected, whereas when λ_{res} of the FP etalon matches the wavelength of excitation or scattering light, a strongly amplified SERS signal can be realized as molecules are located near the Au surface. When the etched dielectric area is immersed in liquids with a distinct RI, an increase or decrease in the Raman intensity is expected in response to the dielectric properties of the layered substrates.

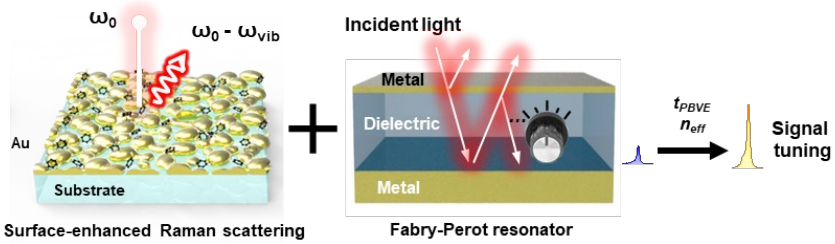

Figure 5.2: Conceptual illustrations of SERS intensities from uniform distribution of randomly dispersed Au nanoparticles and manipulation of nanogap-induced near-field enhancement via Fabry-Perot resonance as a function of dielectric properties of PBVE film.

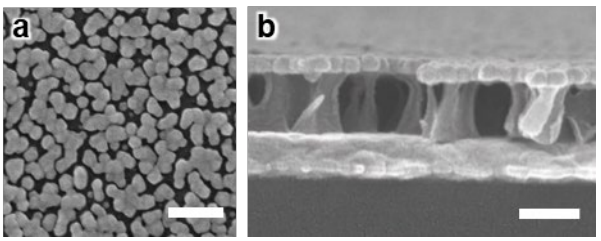

Figure 5.3: Top- (a) and side-view (b) SEM images of FP etalon for tunable Raman substrate.

5.4.2. Maximization of Near-field Raman Enhancement via Au Nanoparticular Assembly

To evaluate the optimal Au nanoarchitecture yielding the maximum near-field enhancement, we explored the morphological and optical characteristics by varying the deposition thickness of the top Au film. Note that only the PBVE film was pre-coated on a transparent glass substrate, followed by different Au deposition thicknesses at a fixed deposition rate and vacuum conditions to focus on the role of Au morphology in the SERS EFs (Fig. 5.4a). The low-density nucleation of Au nanoparticles on the PBVE layer results in an increase in the filling fraction, f_{Au}, of Au proportional to its mass-equivalent thickness (t_{Au}). Top-view SEM images showed that a larger f_{Au} was observed with a thicker t_{Au}. A control experiment was also conducted with a 40-nm-thick Au at a deposition rate of 2.5 Å/s, which clearly emphasized the role of the slow deposition rate (0.3 Å/s) on nanoparticular assembly producing nanoapertures and their growth in size at the same thickness (Fig. 5.4b). Stronger SERS signals arise from either a closer distance between neighboring nanoparticles or a larger number of hotspots with high populations. Thus, the realization of an optimal nanomorphology yielding the maximum SERS signals is highly dependent on the top Au nanostructures. From the results, we found that a slow deposition rate (0.3 Å/s) allowed the formation of nanogaps between neighboring nanoparticles up to t_{Au} = 40 nm over the PBVE surface. Thus, a greater number of hotspots were created without the need for cumbersome and time-intensive chemical treatment [95] or annealing process [96, 97]. The optimum t_{Au} values

were examined using an electric-field distribution simulation to estimate the near-field enhancement from the experimentally obtained SEM images (Fig. 5.5). Simulations were performed to determine the primary factors that affect the improvement of near-field SERS EFs: nanoparticle density, size, and the gap distance between them. The simulation results clearly show that Au nanoparticles prepared with t_{Au} = 30 ~ 40 nm yield the strongest field enhancement, which was confirmed by experimentally measuring the Raman signals of thiophenol absorbed on the Au nanoparticular substrate with varying t_{Au}. Samples were prepared by immersion for 20 min in a 1×10^{-3} M thiophenol solution in ethanol, followed by rinsing for 10 min in pure ethanol. The Raman signals were measured from five randomly chosen spots on the substrate under a 785-nm laser. All SERS measurements were performed under these conditions, unless otherwise stated. Representative Raman spectra measured from thiophenol on Au nanoparticles with different t_{Au} values are displayed in Fig. 5.6a. The simulated electric-field intensity was surface-averaged to plot the quantification values (Fig. 5.6b). The good agreement between the simulated electric-field intensities and the measured SERS signals at a Raman shift of 1573 cm^{-1} (I_{1573}, Fig. 5.6b) implies that a t_{Au} value of 30 or 40 nm is the optimal thickness, yielding maximum near-field enhancements. Larger portions of interconnected Au nanoislands were observed at t_{Au}= 40 nm compared with the case at t_{Au} = 30 nm. Thus, we selected t_{Au}= 40 nm for the optimal t_{Au} values, considering that the reliable and stable nanomorphology construction was expected to have higher sample durability under repeated liquid exposure than that of t_{Au}= 30 nm. For a quantitative evaluation of SERS EF, BPE was drop-

casted on a 40-nm-thick Au substrate (Fig. 5.7) and monitored via Raman spectroscopy, resulting in a SERS EF of 10^6–10^8, which is similar to related studies performed using maskless RIE [17, 98, 99]. Moreover, the transparent nature of the PBVE polymer in the Raman shift range was found to be suitable for the spacer of the etalon by checking SERS signals measured from the front and back sides of the substrate (Fig. 5.8).

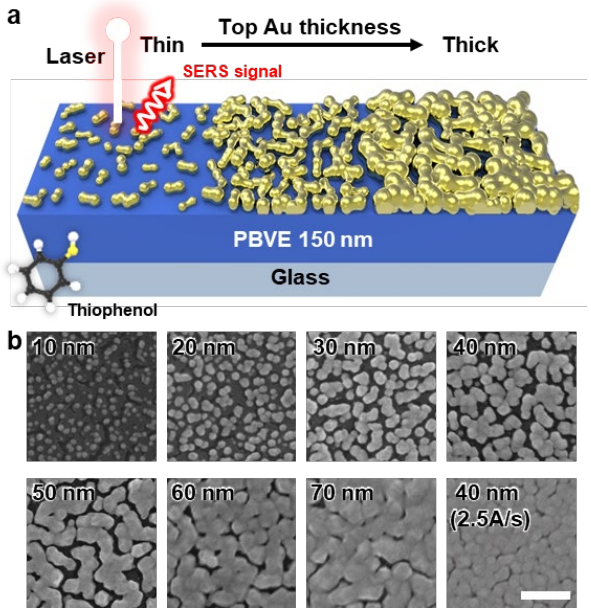

Figure 5.4: Effect of top Au nanoarchitecture on SERS intensity. (a) Schematic description of top Au nanogeometry on the PBVE surface as a function of deposition thickness, t_{Au}. (b) SEM images of thermally deposited Au on the PBVE, varying t_{Au} from 10 nm to 70 nm (constant 0.3 Å/s of deposition rate except for the 2.5 Å/s of control experiment).

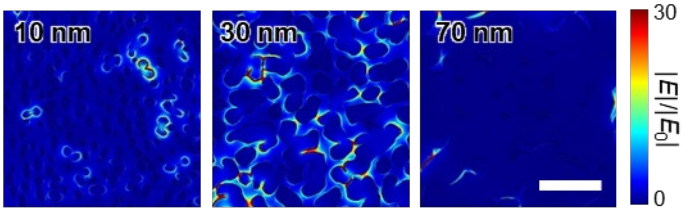

Figure 5.5: Computer simulation showing amplified electric-field distribution on three representative Au structures with t_{Au} values of 10, 30, and 70 nm. Each geometry was sampled from the corresponding SEM images shown in Fig. 5.4b.

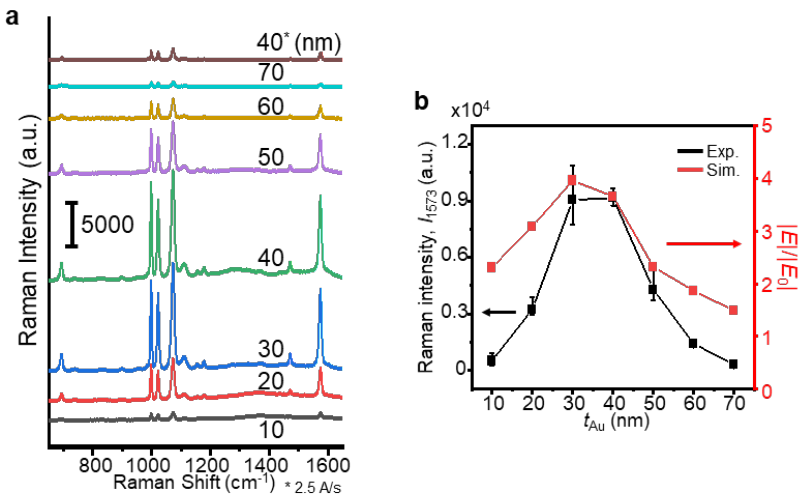

Figure 5.6: (a) Raman spectra of thiophenol measured from the substrates in Fig. 5.5b under 785-nm laser. (b) Plot of Raman intensity at a Raman shift of 1573 cm^{-1} (black) and simulated electric-field intensity at the excitation wavelength 785 nm (red) as a function of t_{Au}. The electric-field intensity was calculated from surface-averaged values on the Au surface.

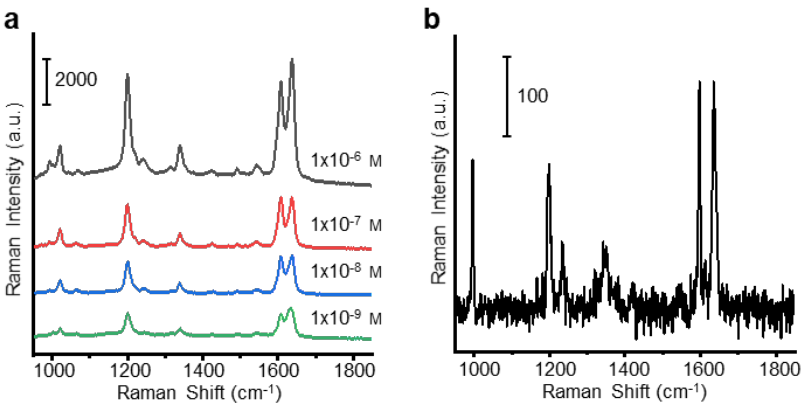

Figure 5.7: Limit of detection for 40-nm-thick nanostructured top Au on a PBVE surface. **(**a) Measured Raman spectra of the BPE molecules at different concentrations adsorbed on a 40-nm-thick Au layer. (b) Measured Raman spectra of BPE on a bare glass. All spectra were averaged from signals of five randomly chosen areas.

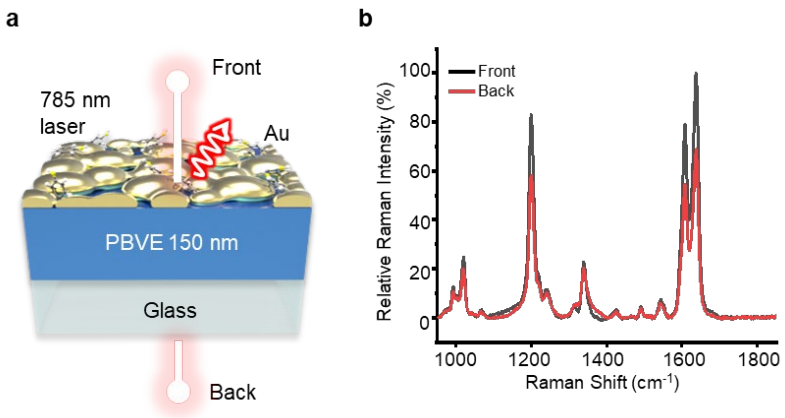

Figure 5.8: Optical transparency of PBVE and Raman spectra collected from the front and back sides. (a) Schematic illustration of Raman measurement on a MD SERS substrate. (b) Measured SERS spectra measured from the front (black) and back (red) sides of the sample. The 1×10^{-6} M BPE molecules were drop-casted and dried prior to the measurement. The result shows that the Raman intensity from the back side is ~70 % less than that from the front.

5.4.3. Modulation of Far-field Raman Enhancement Effect via Dielectric Tuning

After establishing the optimal t_{Au} for maximizing the near-field SERS effect, we prepared a MDM etalon for the FP cavity architecture by applying a 120-nm-thick Au mirror film underneath the PBVE layer. In chapter 3, it was m that the FP resonance of an MDM etalon depends on the thickness (t_{PBVE}) and effective RI (n_{eff}) of the dielectric layers. Because λ_{res} originates from a particular wavelength absorption at the FP, we propose that the far-field enhancement interacts with the structural properties of the FP etalon, t_{PBVE}, and n_{eff}. To confirm this, Au-PBVE-Au etalons with different t_{PBVE} values were prepared by adjusting the spin-coating conditions (Fig. 5.9). The resonance dips of λ_{res} tended to red-shift as t_{PBVE} increased (Fig. 5.10a). For example, the FP sample with t_{PBVE} = 175 nm exhibited a resonance dip at λ_{res} = 680 nm. Then, the resonance dip shifted to the infrared range, passing through 785 nm (the wavelength of the Raman laser source), while t_{PBVE} increased to 335 nm.

To accurately predict the far-field enhancement of the FP etalon, we displayed a heat map indicating cavity EF as a function of t_{PBVE} using FEM simulations (Fig. 5.10b). Unlike randomly dispersed Au nanoparticles, FP resonance has a relatively sharp resonance wavelength. As represented in Eq. (1.1), the SERS EF is highly dependent on the electric field intensity at λ_{ex} and λ_{sc}, implying that cavity EFs vary with λ_{ex}, λ_{sc}, and t_{PBVE}. In the simulation, the top Au nanostructure was modeled as a single-material film based on effective medium theory [100] to identify the effect of optical interference. Note that the

top film of the FP cavity was heterogeneous: a mixture of Au metal and air with f_{Au} = 0.65. The simulated far-field SERS EFs at 1573 cm^{-1} (λ_{sc} = 895 nm) as a function of t_{PBVE} are plotted in the red curve in Figure 3d. For the experimental measurements, thiophenol was applied to the top Au film, and Raman peak intensities at 1573 cm^{-1} (I_{1573}) were displayed along with the cavity EF at 1573 cm^{-1}. Both the experimental and simulation results show that there is a dramatic decline in the Raman enhancement over t_{PBVE} > 240 nm, which provides an insight into the practical application of our FP etalon as a "Raman switch" for SERS signal on/off. Moreover, the two dips in t_{PBVE} between 230 nm and 300 nm show that constructive interference affects individual Raman signals as they pass through λ_{ex} and λ_{sc} (Fig. 5.11).

The top Au nanoparticles perform multifunctional roles not only as optical hotspots for the near-field enhancement effect but also as a shadow mask for the creation of air pockets in the dielectric film via the RIE process. Through directional etching of the dielectric layer, the n_{eff} value of the dielectric layer can be adjusted, thereby modulating the far-field SERS EF. The FP sample with t_{PBVE} = 240 nm underwent O_2 RIE from 0 s to 45 s at 15 s intervals, confirming the blue-shift of λ_{res} as the etching duration increased (Fig. 5.12a). This indicates that the thinning effect of the PBVE was caused by an increased amount of air. Note that n_{air} is 1, and n_{eff} of the dielectric layer is the effective value between n_{air} and n_{PBVE}. The experimental SERS intensity of thiophenol adsorbed in each FP etalon with different etching durations confirms that the 45 s etched FP etalon with $\lambda_{res} \approx$ 785 nm shows the strongest SERS intensity under 785-nm laser illumination (Fig. 5.12b). Figure 5.12c shows that the longer the time for

which the dielectric film was etched, the stronger the SERS signals that were measured. In addition, the excellent agreement between the simulation and experimental data shows that the maximum far-field SERS effect is expected when the FP etalon producing λ_{res} (at t_{PBVE} = 240 nm by 45 s etching duration) matches the excitation and scattering wavelengths. Collectively, the optical path length control across the dielectric layer can modulate the overall SERS intensity, causing far-field enhancement tuning as it provides an opportunity for the realization of a new dynamic Raman scattering technology. Quantitative measurements using BPE also revealed an enhancement effect of optical interference (Fig. 5.13).

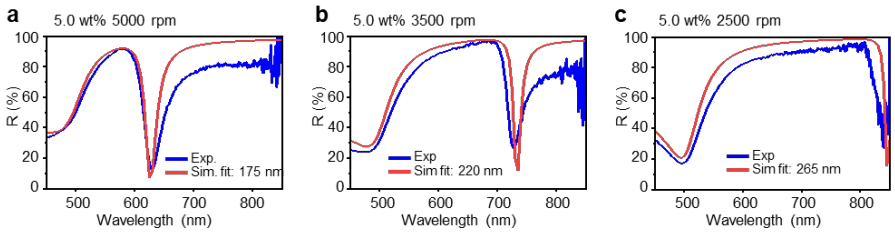

Figure 5.9: Examples of measurement fitting to estimate t_{PBVE}. (a-c) Experimentally measured reflectance (blue) and simulated reflectance (red) on the MDM structure with flat top Au films.

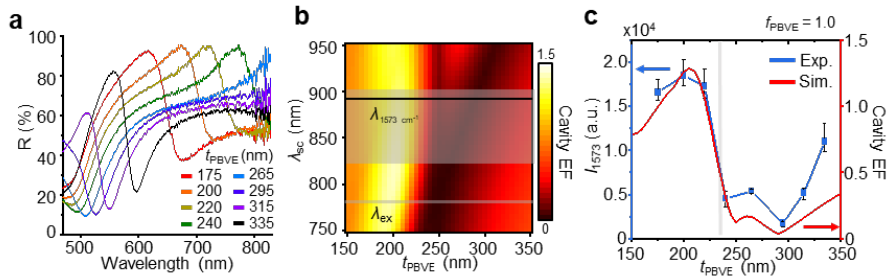

Figure 5.10: (a) Measured reflective spectra for different dielectric layer thicknesses with varying t_{PBVE}. (b) Simulated SERS EF in FP cavity (cavity EF) with distinct t_{PBVE}. (c) Measured SERS intensity and simulated cavity EF at the 1573 cm^{-1} as a function of t_{PBVE}.

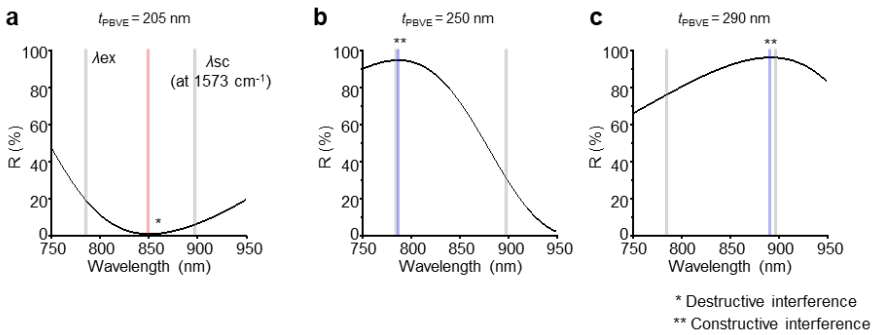

Figure 5.11: (a-c) Simulated reflectances at t_{PBVE}= 205, 250, and 290 nm to compare the excitation (λ_{ex}) and scattering wavelengths (λ_{sc})**.** The cavity EF is maximized when t_{PBVE} = 205 nm as the spectral position of the dip is placed between λ_{ex} and λ_{sc} (a). Meanwhile, the minimum points of cavity EF correspond to t_{PBVE} = 250 and 290 nm having constructive interferences at λ_{ex} and λ_{sc}, respectively (b, c). The optical measurements intuitively display the correlation between the optical interferences and cavity EF.

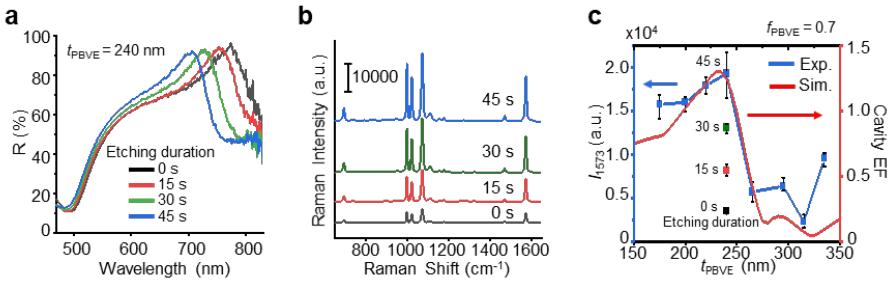

Figure 5.12: (a) Reflectance spectra with etching durations ranging from 0 to 45 s (t_{PBVE} = 240 nm). (b) SERS performance of the dielectric layer tailored substrates for varying etching durations. (c) SERS signal and cavity EF shifts at the 1573 cm-$^{-1}$ as a function of t_{PBVE}. Black, red, green, and blue dots represent the measured SERS intensity with etching durations of 0, 15, 30, and 45 s.

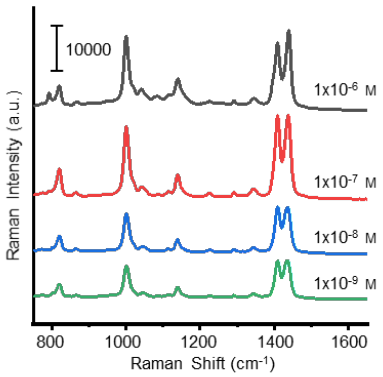

Figure 5.13: Detection limit of MDM SERS device. SERS spectra of BPE molecules on the MDM structure**.** The samples were prepared with t_{PBVE} of 240 nm and etching duration of 45 s. The SERS EF values at 1200 cm^{-1} are increased to 1.31×10^{7} (1×10^{-6} M) and 6.22×10^{9} (1×10^{-9} M).

5.4.4. Dynamic SERS Signal Tuning via Dielectric Modulation

The physicochemical modulation of the dielectric properties affects the functionality of the analytical devices, that is, a change in the magnitude of the SERS signals. The nanoapertures of the top Au film enable spatial etching of the dielectric film, resulting in optical (or physicochemical) tuning via the exchange of a portion of the PBVE polymer with air as it forms air voids. To show the role of air voids in response to external media, a negative control experiment was conducted using a non-etched MDM etalon. It is assumed that the amount of thiophenol adsorbed on the Au surface is constant regardless of the medium owing to the high-affinity binding between the Au and S atoms [101]. When the surrounding environment was changed from air (n = 1.0) to ethanol (n = 1.33), the effect on the reflectance of the device was minimal (Fig. 5.14a). However, the SERS signal was reduced by approximately one-third (Fig. 5.14b), indicating a decreased electric-field intensity depending on the permittivity of the external medium (air to ethanol). Next, an MDM etalon with f_{PBVE} = 0.7 confirmed the infiltration of ethanol inside the dielectric layer through the red shifts of λ_{res} (Fig. 5.14c), accompanied by a decrease in SERS signals under ethanol exposure (Fig. 5.14d). Because ethanol immersion entirely lowers the cavity EF (Fig. 5.15a *vs.* Fig. 5.10b) and restores λ_{res} to the non-etched state, the dynamic variation of the SERS signal is caused by both ethanol and dielectric etching, showing its weakening and strengthening effects, respectively (Fig. 5.15b). The simulation and experimental results for ethanol

were consistent as a function of t_{PBVE} (Fig. 5.16). The uniformity of the MDM etalon was evaluated by partial etching of the PBVE film (f_{PBVE} = 1.0 for the left-side and 0.7 for the right-side of the sample, Fig. 5.15c) and measured zone-sensitive SERS signals at 1573 cm^{-1} (I_{1573}) by mapping the molecular signal intensities. The mapping images were obtained at an exposure time of 0.5 s and a lateral resolution of 300 μm. The relative standard deviation (RSD) values calculated from each area, etched (9.6%) and non-etched (19.1%) areas, confirmed the structural uniformity of the MDM etalon, which was also validated by mapping at a smaller step size of 20 μm (Fig. 5.17). Interestingly, the strongly enhanced SERS signals at the etched area were turned off by ethanol immersion (Fig. 5.15d), which indicates that the medium exchange can provide a clue for the realization of the MDM etalon as a signal switch. The detailed effect and working principle of liquid infiltration for SERS signal modulation were addressed together with repeatable and switchable optical performances (Fig. 5.18). The results demonstrated that cavity control (either dielectric etching or exposure to liquids) plays a critical role in tunable Raman scattering.

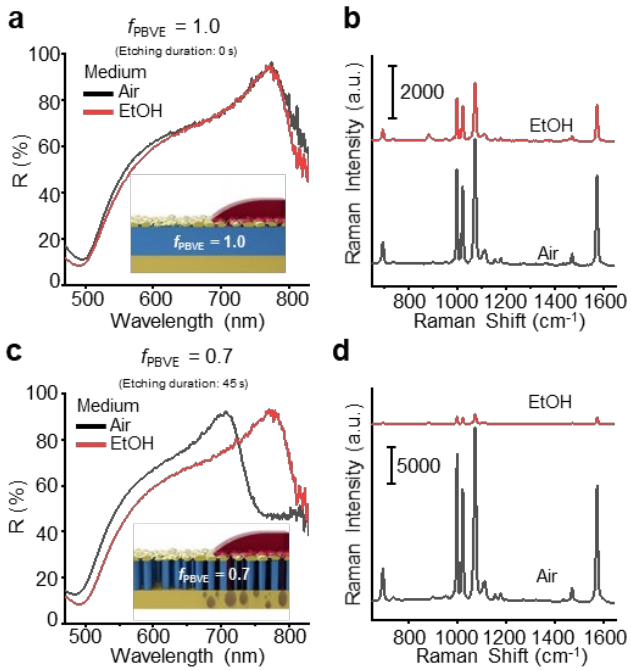

Figure 5.14: Measured reflectance spectra (a, c) and SERS spectra (b, d) of thiophenol absorbed on nanostructured Au layer under media of n = 1.0 (Air) and n = 1.33 (ethanol; EtOH) with inset showing schematics; t_{PBVE} = 240 nm, non-etched structure (a) and etched structure (c).

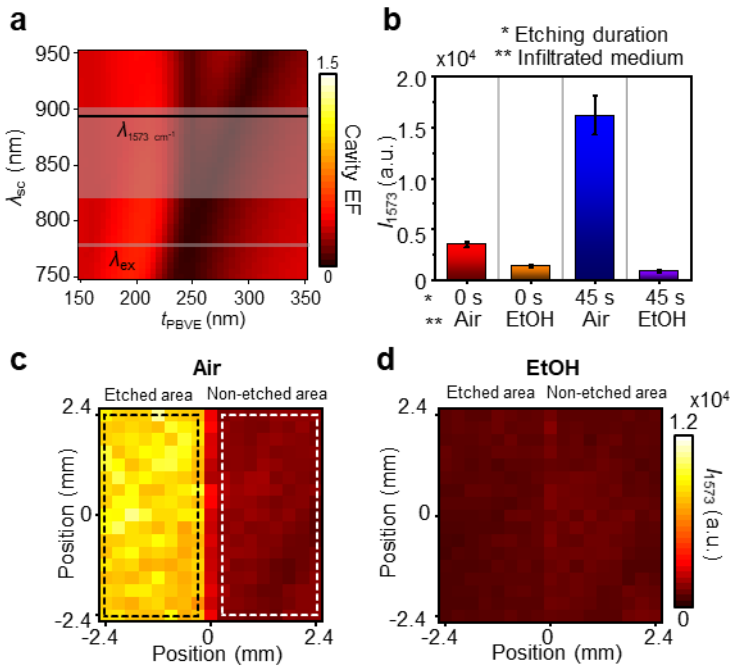

Figure 5.15: (a) Simulated cavity EF with ethanol immersion. (b) Comparison of SERS intensity at 1573 cm^{-1} (I_{1573}) with PBVE volume fraction (f_{PBVE} = 1.0 and 0.7) and infiltrated media (Air and EtOH). (c, d) Raman mapping of thiophenol obtained on partially etched MDM substrate under media of Air (c) and EtOH (d).

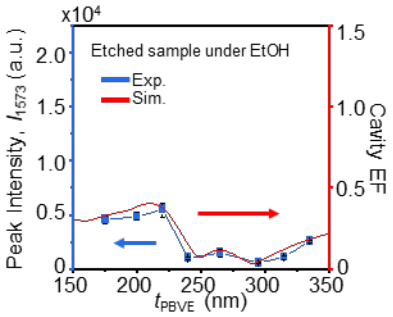

Figure 5.16: Measured SERS intensity and simulated cavity EF at 1573 cm^{-1} under ethanol (EtOH, n = 1.33).

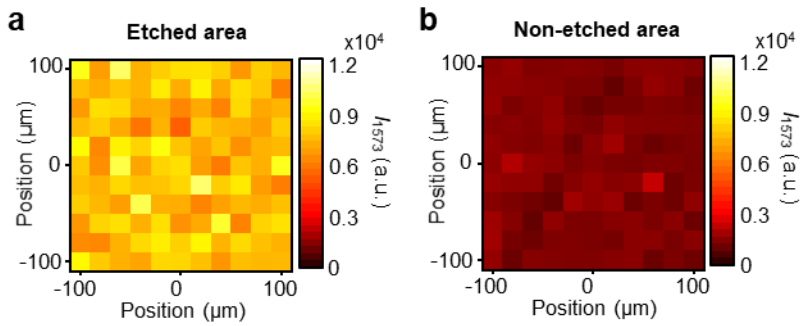

Figure 5.17: Uniformity of MDM SERS etalon. **(**a, b) The Raman mapping images were obtained with a step size of 20 μm. The relative standard deviations (RSD) values are 12.5 % and 17.9 % on etched (a) and non-etched (b) areas, respectively.

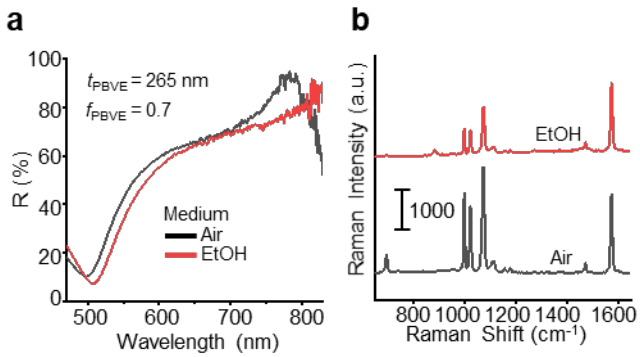

Figure 5.18: Raman intensity modulation via liquid infiltration. (a), Measured reflectance spectra from MDM etalon consisting of t_{Bottom_Au} = 120 nm, t_{top_Au} = 40 nm, t_{PBVE} = 265 nm and PBVE volume fraction, f_{PBVE} = 0.7 under air (black) and ethanol (red). (b) Measured Raman spectra of thiophenol adsorbed on the MDM etalon shown in (a). The Raman intensity at 694 cm^{-1} is notably decreased under ethanol compared with that at 1573 cm^{-1} because the spectral position of the constructive interference is matched to λ_{sc} (at 694 cm^{-1}).

5.4.5. Raman message encryption via FP etalon-based dynamic SERS substrate

To test the dynamic and tunable SERS signals for practical applications, multiple Raman probes-encoded MDM etalons was prepared to examine whether the application of dielectric modulation followed by liquid immersion is suitable for information displaying/hiding modulators using Raman measurements. Dielectric etching changes the reflective colors of the encoded information ("KIST," Fig. 5.19), and a Raman mapping technique displays zone-sensitive Raman signals with different species as well as magnitudes depending on the dielectric properties of the FP etalon. The MDM etalon with t_{PBVE} = 240 nm was prepared because it showed the minimum SERS signals for f_{PBVE} = 1.0 and the maximum SERS signals when etched for f_{PBVE} = 0.7. Besides, two kinds of Raman probes, 3-methoxythiophenol and thiophenol, were coated in a site-selective manner using a shadow mask for encoding distinct information (*i.e.*, red "K," "S" and blue "I," "T"). Because O_2 plasma damages most organic compounds, both the PBVE dielectric layer and pre-coated 3-methoxythiophenol adsorbed on the top Au layer were removed during the RIE process. Sequential exposure of thiophenol backfilled the analyte-free zone (Fig. 5.20). When measured in dry conditions, distinguished SERS spectra measured from each "K," "I," "S," "T," and background area demonstrated that the MDM etalon was prepared with different species and geometries (Fig. 5.21a). Stronger Raman signals were measured in "K" and "I" (45 s etching) than in "S" and "T" (30 s etching). Mapping of the characteristic peak intensity shows only a clear

"K" and a bit dimmed "S" at 1608 cm^{-1} (Fig. 5.21b), while showing only "I" and "T" at 999 cm^{-1} in the same manner (Fig. 5.21c). All SERS modulations based on dielectric tuning and different Raman probes could be simply switched off by immersing the substrate in ethanol (Fig. 5.22). As the external medium is exchanged from air to ethanol, the regional optical and electrical variations vanish immediately, hiding all encrypted information (both visual and Raman interpreted). This successfully demonstrates that the proposed MDM etalon can deliver diverse information that requires both optical and chemical interpretation with dynamic hiding.

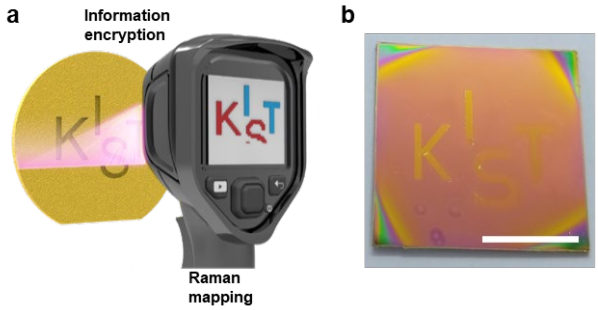

Figure 5.19: Conceptual illustration (a) and photograph (b) of the prepared FP sample for message encryption by SERS mapping. Scale bar, 1cm.

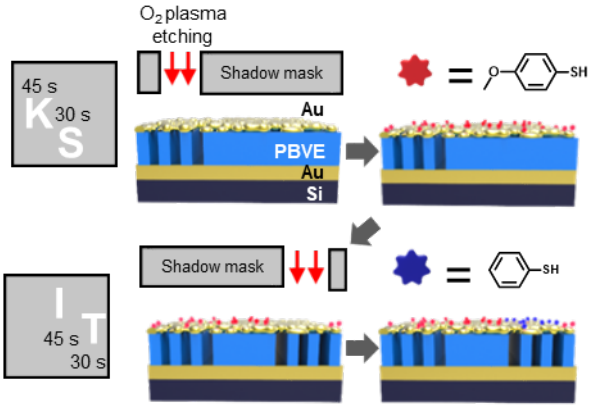

Figure 5.20: Fabrication process for engraving message via Au-S bonding of different Raman probe molecules.

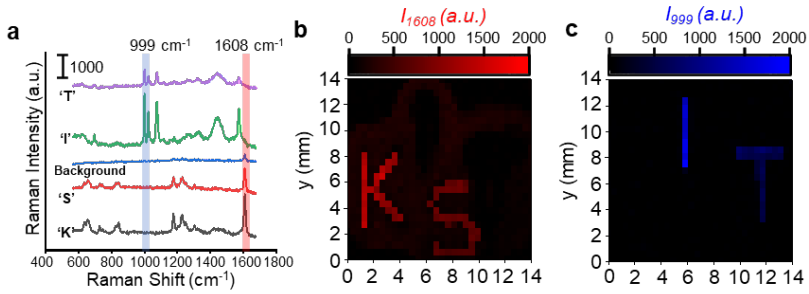

Figure 5.21: Raman spectrum (a) and Raman mapping images plotted for the 1608 cm^{-1} (b) and 999 cm^{-1} (c) for SERS signal tuning via dielectric modulation under air. Raman bands represent intrinsic peaks for 3-methoxythiophenol and thiophenol.

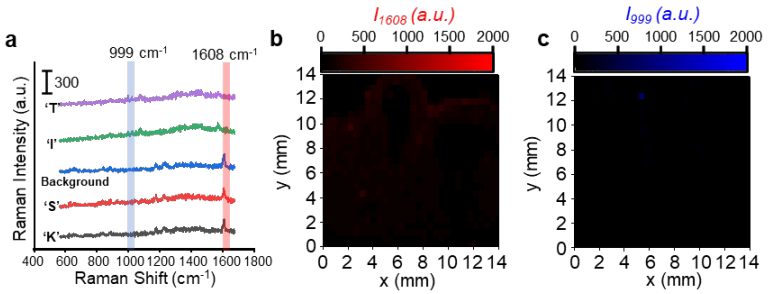

Figure 5.22: Raman spectrum (a) and Raman mapping images plotted for the 1608 cm^{-1} (b) and 999 cm^{-1} (c) for SERS signal tuning via dielectric modulation under ethanol. Raman bands represent intrinsic peaks for 3-methoxythiophenol and thiophenol.

5.5. Summary

In this chapter, the dynamic plasmonic SERS effect was verified by performing thorough computational simulations and experimental proofs: near-field optimization via Au nanoparticle assembly and far-field manipulation by optical interference (λ_{res}) tuning. The analytical performance of the Raman probes absorbed at the top metal film was tuned by either the physical (f_{PBVE}) or chemical (by air or ethanol infiltration) properties of the dielectric film. The dynamic SERS EF changes in response to external liquids have expanded their application as a "Raman switch" for developing information encryption.

The MDM etalon produces unique optical characteristics that tune the overall performance of the analytical devices by controlling the far-field EF and near-field EF. Because closer nanogaps and more populated hotspots yield a higher near-field SERS effect, the development of a simple fabrication method that produces highly populated nanogaps is one of the mainstream methods for achieving a low LoD. Maskless RIE [17, 98, 99], chemically synthesized nanowires [102], and thermal dewetting [96, 97] methods have been reported for the construction of nanostructured substrates with abundant nanogaps. Meanwhile, fine structures with sophisticated designs yield not only near-field SERS effects but also sharp far-field profiles owing to their periodically arranged subwavelength structures. Thus, a thorough understanding of the correlation between the near-field Raman enhancement and far-field response is essential for the successful development of SERS-based analytical platforms. The strategy of positioning a mirror metal underneath the near-field generating optical hotspots creates an additional tuning factor, that is, the far-field SERS

EF, by generating a tunable resonance frequency without a loss of the near-field SERS EF. Experimentally, FP interference leads to additional amplification of the SERS signals achieved from near-field EFs by factors of three to four times (MD and MDM structures exhibited SERS EFs of 10^6–10^8 and 10^7–10^9, respectively). Furthermore, its dynamic SERS enhancement tunability as well as SERS reduction enables the establishment of SERS signal cancelation, which plays an essential role in realizing the dynamic "Raman switch." Further, the Raman peak of the target analytes can be either emphasized or diminished depending on whether λ_{res} matches the λ_{sc} of the peak. This could lead to the creation of an analytic multi-specimen SERS chip, which could allow fundamental research to a mass scientific knowledge while simultaneously meeting industrial demands

Chapter 6. Concluding Remarks

In this thesis, a precise control of nanoscale thin film etalon is presented for a wide range application of colorimeter sensors and molecular analysis tools. The general overview about light-matter interaction, structural coloration by MDM structures and SERS is briefly introduced in **Chapter 1**, and more detailed theoretical backgrounds are addressed in **Chapter 2**. Three research works about the extraordinary MDM etalon with nanostructures are reported with throughout computational and experimental analysis and results in the next three chapters, respsectively.

In **Chapter 3**, the effect of each composing layer to etalon's structural color is deeply studied. Controllable parameters such as thickness and filling fraction of metals and polymer dielectrics were precisely adjusted to provide a wide range of visible color generation. Due to the low surface energy of the fluorinated polymer dielectric layer, nano-perforated top metal and additional nano-cavity formation are cost-effectively obtained. The comprehensive liquid-sensitive characteristics of the MDM etalon, which can not only be tuned through refractive index but also surface tension, can be used as various routes of optical coloration applications such as environment-sensitive smart mirrors, humidity sensors, and other smart display techniques. Moreover, the proposed structure can be applied to the liquid-sensitive anti-counterfeiting display or optical camouflage displays to deliver hidden information for security purpose.

In **Chapter 4**, the gas-permeable top metal and polymer dielectric layers allow catalytic gas reaction at their interface. Previous reports demonstrated simultaneous generation and subsequent nanoscale water-forming reaction of hydrogen and oxygen on the Pd metal catalyst using electro-potential devices [72, 73]. Recently, optical monitoring of such water films and their 2-dimensional growth were imaged between a vitreous silicon dioxide bilayer and ruthenium [103]. However, observation of the local position and growth rates of water film formation is prohibited, eliminating any possible measurement for quantitative analysis of the transition metals. Here, the polymer layer suppresses the water evaporation rate and enables to grow the produced water bubbles and films thick enough for naked-eye observation. Moreover, metal hydrogenation has been investigated using diverse materials to realize repeatable and reliable coloration devices. Magnesium (Mg) or yttrium (Y), as representative hydrogen absorbents, showed phase transformation from the metallic phase to dielectric MgH_2 or YH_X, as it promotes dynamic plasmonic coloration with remarkable variations in reflectance spectra [104, 105]. However, these coloration techniques are highly dependent on material properties and have insuperable disadvantages such as low switching speed, inferior color tunability, and low color efficiency. Although the induced phase change of the gas-sensitive Mg-assisted FP etalon is the most sophisticated and advanced dynamic coloration technology to date, it still suffers from material stability and safety issues when exposed to moisture (humid environment) which is crucial for industrial applications. Unlike any other dynamic color tuning strategy using metal hydride-based reports, the proposed FP etalon

shows superior stability (≥ 28 times) of the device structures. The advanced repetition without active metal damage is because the color change did not originate from the direct reaction of the Pd/PdH transition but the water-forming reaction at the PBVE/Pd interfaces. Overall, employing the colorimetric display for monitoring different chemical reactions at catalytic interfaces creates numerous opportunities to clarify the underlying physics, chemistry, and applied surface chemistry assisted by optoelectronic nanostructures. For example, the advanced photonic measurement for the 'membrane permeability test' of polymers of interest. Without state-of-the-art imaging instruments, we can avoid the diffraction limit of measurements and monitor the pathway solely on color variation. Smart windows for air quality monitoring or gas leaking warning displays can be other applicable areas as they meet industrial needs owing to their scalable and simple fabrication process with diverse solid supports and various metal selections.

In **Chapter 5**, the randomly dispersed nanogap among top Au film is suitable for near-field SERS effect, and the strategy of matching optical interference to the excitation and scattering wavelengths can be applied to the development of multi-laser and multi-specimen SERS chips for maximizing the far-field Raman signals of each specimen. For example, an FP etalon with λ_{res} = 785 nm can be zone-selectively tuned to 633 nm to match the λ_{ex} values of distinct laser sources on the same SERS substrate. In addition, it can resonate with multiple lights via high-order modes and can be coupled with photonic materials encapsulated in the cavity. This structural advantage of easy accessibility of the external medium into the cavity makes it a promising

platform for observing extraordinary optical phenomena such as Rabi splitting [106-108], excitation transfer [109], and metal-enhanced fluorescence [110]. Furthermore, cost-effective and scalable fabrication processes of MDM substrates are suitable for practical applications, including information encryption [111-113], cell analysis [114], drug delivery analysis [115], and stimulus-responsive Raman detection [116].

Utilization and proficient manipulation of visible colors are powerful tools to deliver information to others in various industries. The thin film optic devices, MDM etalons, studied in this thesis are promising optical platforms for diverse fields of scientific researches and practical applications because of their simple structure, easy fabrication, tunability and dynamicity. The research findings introduced in this thesis would help promoting potential convergences of different fields of science and engineering.

Acronyms

BEMT: Bruggeman's effective medium theory

BPE: 1,2-bis(4-pyridyl)ethylene

DFT: Density functional theory

DI water: De-ionized water

EF: Enhancement factor

EM: Electromagnetic

EtOH: Ethanol

FEM: Finite-element method

FITC: Fluorescein isothiocyanate

FL: Fluorescence

FLIC: Fluorescence interference contrast microscopy

FP: Fabry-Perot

LoD: Limit of detection

MDM: Metal-dielectric-metal

MFC: Mass flow controller

PBVE: perfluoro-(butenyl vinyl ether)

PMMA: polymethyl methacrylate

RSD: Relative standard deviation

SEM: Scanning electron microscope

SERS: Surface-enhanced Raman scattering

RI: Refractive index

RIE: Reactive ion etching

TMM: Transfer matric method

1D: One-dimensional

2D: Two-dimensional

3D: Three-dimensional

Bibliography

1. Lu, H., Ren, X., Ouyang, D., & Choy, W. C. Emerging novel metal electrodes for photovoltaic applications. *Small* **14**, 1703140 (2018).
2. Huang, C. Z., & Li, Y. F. Resonance light scattering technique used for biochemical and pharmaceutical analysis. *Analytica chimica acta* **500**, 105-117 (2003).
3. Roke, S., & Gonella, G. Nonlinear light scattering and spectroscopy of particles and droplets in liquids. *Annual review of physical chemistry* **63**, 353-378 (2012).
4. Yang, L., Lenz, R., & Kruse, B. Light scattering and ink penetration effects on tone reproduction. *JOSA A* **18**, 360-366 (2001).
5. Hillenbrand, R., Taubner, T., & Keilmann, F. Phonon-enhanced light–matter interaction at the nanometre scale. *Nature* **418**, 159-162 (2002).
6. Shu, F. Z. *et al.* Dynamic plasmonic color generation based on phase transition of vanadium dioxide. *Advanced Optical Materials* **6**, 1700939 (2018).
7. Fudouzi, H., & Sawada, T. Photonic rubber sheets with tunable color by elastic deformation. *Langmuir* **22**, 1365-1368 (2006).
8. Jung, C. *et al.* Disordered-nanoparticle–based etalon for ultrafast humidity-responsive colorimetric sensors and anti-counterfeiting displays. *Science Advances* **8**, eabm8598 (2022).
9. De La Rica, R., & Stevens, M. M. Plasmonic ELSIA for the ultrasensitive detection of disease biomarkers with the naked eye. *Nature nanotechnology* **7**, 821-824 (2012).
10. Duan, X., & Liu, N. Scanning plasmonic color display. *ACS Nano* **12**, 8817-8823 (2018).
11. Khatua, S. *et al.* Plasmonic nanoparticles− liquid crystal composites. *The Journal of Physical Chemistry C* **114**, 7251-7257 (2010).

12. Araki, S., Nakamura, K., Kobayashi, K., Tsuboi, A., & Kobayashi, N. Electrochemical optical-modulation device with reversible transformation between transparent, mirror, and black. *Advanced Materials* **24**, OP122-OP126 (2012).
13. Thakur, V. K., Ding, G., Ma, J., Lee, P. S., & Lu, X. Hybrid materials and polymer electrolytes for electrochromic device applications. *Advanced Materials* **24**, 4071-4096 (2012).
14. Neubrech, F., Duan, X., & Liu, N. Dynamic plasmonic color generation enabled by functional materials. *Science Advances* **6**, eabc2709 (2020).
15. Qian, X.-M., & Nie, S. M. Single-molecule and single-nanoparticle SERS: from fundamental mechanisms to biomedical applications. *Chemical Society Reviews* **37**, 912-920 (2008).
16. Nam, J.-M., Oh, J.-W., Lee, H., & Suh, Y. D. Plasmonic nanogap-enhanced Raman scattering with nanoparticles. *Accounts of chemical research* **49**, 2746-2755 (2016).
17. Wu, K., Nguyen, L. Q., Rindzevicius, T., Keller, S. S., & Boisen, A. Wafer-scale polymer-based transparent nanocorals with excellent nanoplasmonic photothermal stability for high-power and superfast SERS imaging. *Advanced Optical Materials* **7**, 1901413 (2019).
18. Kang, M., Park, S.-G., & Jeong, K.-H. Repeated solid-state dewetting of thin gold films for nanogap-rich plasmonic nanoislands. *Scientific reports* **5**, 14790 (2015).
19. Sun, J. Y., Bhushan, B., & Tong, J. Structural coloration in nature. *RSC advances* **3**, 14862-14889 (2013).
20. Freestone, I., Meeks, N., Sax, M., & Higgitt, C. The Lycurgus cup - a roman nanotechnology. *Gold bulletin* **40**, 270-277 (2007).
21. Dammann, H. Color separation gratings. *Appliled Optics* **17**, 2273-2279 (1978).

22. Yablonovitch, E. Inhibited spontaneous emission in solid-state physics and electronics. *Physical review letters* **58**, 2059-2062 (1987).
23. Serpe, M. J., Kang, Y., & Zhang, Q. M. *Photonic materials for sensing, biosensing and display devices. Springer Series in Materials Science.* (Springer, 2016).
24. Kim, J. H., Moon, J. H., Lee, S. Y., & Park, J. Biologically inspired humidity sensor based on three-dimensional photonic crystals. *Applied Physics Letters* **97**, 103701 (2010).
25. Landy, N. I., Sajuyigbe, S., Mock, J. J., Smith, D. R., & Padilla, W. J. Perfect metamaterial absorber. *Physical review letters* **100**, 207402 (2008).
26. Do, Y. S. *et al.* Plasmonic color filter and its fabrication for large-area applications. *Advanced Optical Materials* **1**, 133-138 (2013).
27. Nam, H., Song, K., Ha, D., & Kim, T. Inkjet printing based mono-layered photonic crystal patterning for anti-counterfeiting structural colors. *Scientific reports* **6**, 30885 (2016).
28. Nath, N., & Chilkoti, A. A colorimetric gold nanoparticle sensor to interrogate biomolecular interactions in real time on a surface. *Analytical chemistry* **74**, 504-509 (2002).
29. Pursiainen, O. L. J. *et al.* Nanoparticle-tuned structural color from polymer opals. *Optics Express* **15**, 9553-9561 (2007).
30. Chen, Y. Nanofabrication by electron beam lithography and its applications: a review. *Microelectronic Engineering* **135**, 57-72 (2015).
31. Ji, T. *et al.* Plasmonic broadband absorber by stacking multiple metallic nanoparticle layers. *Applied Physics Letters* **106**, 161107 (2015).
32. Ehlert, O., Thomann, R., Darbandi, M., & Nann, T. A four-color colloidal multiplexing nanoparticle system. *ACS Nano* **2**, 120-124 (2008).
33. Bruggeman, D. A. G. The calculation of various physical constants of heterogeneous substances. I. The dielectric constants and conductivities of

mixtures composed of isotropic substances. *Annals of Physics* **416**, 636-791 (1935).

34. Liu, Z. Q. *et al.* Automatically acquired broadband plasmonic-metamaterial black absorber during the metallic film-formation. *ACS applied materials & interfaces* **7**, 4962-4968 (2015).
35. Yu, E. S. *et al.* Highly sensitive color tunablility by scalable nanomorphology of a dielectric layer in liquid-permeable metal- insulator-metal structure. *ACS applied materials & interfaces* **10**, 38581-38587 (2018).
36. Kim, S.-J., Choi, H.-K., Lee, H., & Hong, S.-H. Solution-processable nanocrystal-based broadband Fabry–Perot absorber for reflective vivid color generation. *ACS applied materials & interfaces* **11**, 7280-7287 (2019).
37. Balčytis, A. *et al.* From fundamental toward applied SERS: shared principles and divergent approaches. *Advanced Optical Materials* **6**, 1800292 (2018).
38. Wang, X., Huang, S.-C., Hu, S., Yan, S., & Ren, B. Fundamental understanding and applications of plasmon-enhanced Raman spectroscopy. *Nature Reviews Physics* **2**, 253-271 (2020).
39. Nguyen, M. *et al.* Dynamic plasmonic platform to investigate the correlation between far-field optical response and SERS signal of analytes. *ACS omega* **4**, 1144-1150 (2019).
40. Hering, K. *et al.* SERS: a versatile tool in chemical and biochemical diagnostics. *Analytical and bioanalytical chemistry* **390**, 113-124 (2008).
41. Wei, H., Abtahi, S. M. H., & Vikesland, P. J. Plasmonic colorimetric and SERS sensors for environmental analysis. *Environmental Science: Nano* **2**, 120-135 (2015).
42. Yaseen, T., Pu, H., & Sun, D.-W. Functionalization techniques for improving SERS substrates and their applications in food safety evaluation:

a review of recent research trends. *Trends in food science & technology* **72**, 162-174 (2018).

43. Zhou, Y. *et al.* Multiplexed SERS barcodes for anti-counterfeiting. *ACS applied materials & interfaces* **12**, 28532-28538 (2020).
44. Saleh, B. E., & Teich, M. C. *Fundamentals of photonics*. (John Wiley & Sons, 2019).
45. Markoš, P., & Soukoulis, C. *Wave propagation. From electrons to photonic crystals and left-handed materials.* (Princeton University Press, 2008).
46. Fowles, G. R. *Introduction to modern optics*. (Courier Corporation, 1989).
47. Cai, W., & Shalaev, V. M. *Optical metamaterials*, vol. 10. (Springer, 2010).
48. Hess, C. New advances in using Raman spectroscopy for the characterization of catalysts and catalytic reactions. *Chemical Society Reviews* **50**, 3519-3564 (2021).
49. Lee, I.-H., Lee, S.-H., Keum, C.-M., Kim, S.-U., & Lee, S.-D. Combinatorial color arrays based on optical micro-resonators in monolithic architecture. *Optics Express* **22**, 15320-15327 (2014).
50. Lee, I.-H., Yu, E.-S., Lee, S.-H., & Lee, S.-D. Full-coloration based on metallic nanostructures through phase discontinuity in Fabry-Perot resonators. *Optics Express* **27**, 33098-33110 (2019).
51. Kim, T. *et al.* Asymmetric optical camouflage: Tuneable reflective colour accompanied by the optical Janus effect. *Light: Science & Applications* **9**, 175 (2020).
52. Jang, J. *et al.* Spectral modulation through the hybridization of mie-scatterers and quasi-guided mode resonances: realizing full and gradients of structural color. *ACS Nano* **14**, 15317-15326 (2020).
53. Qiu, Y. L., Yang, S., & Sheng, K. Photolithographic patterning of cytop with limited contact angle degradation. *Micromachines* **9**, 509 (2018).

54. Jeong, H.-D. *et al.* Physicochemical modulation of nanometer-thick etalon films for liquid-sensitive color display with full-color spectrum generation. *ACS Applied Nano Materials* **4**, 389-395 (2020).
55. Andringa, A. M. *et al.* Gate-bias controlled charge trapping as a mechanism for NO_2 detection with field-effect transistors. *Advanced Functional Materials.* **21**, 100-107 (2011).
56. Georg, A., Georg, A., Graf, W., & Wittwer, V. Switchable windows with tungsten oxide. *Vacuum* **82**, 730-735 (2008).
57. Huiberts, J. *et al.* Yttrium and lanthanum hydride films with switchable optical properties. *Nature* **380**, 231-234 (1996).
58. Palm, K. J., Murray, J. B., Narayan, T. C., & Munday, J. N. Dynamic optical properties of metal hydrides. *ACS Photonics* **5**, 4677-4686 (2018).
59. Nørskov, J. K., Abild-Pedersen, F., Studt, F., & Bligaard, T. Density functional theory in surface chemistry and catalysis. *Proceedings of the National Academy of Science* **108**, 937-943 (2011).
60. Rotermund, H., Ertl, G., & Sesselmann, W. Scanning photoemission microscopy of surfaces. *Surface science* **217**, L383-L390 (1989).
61. Telieps, W., & Bauer, E. An analytical reflection and emission UHV surface electron microscope. *Ultramicroscopy* **17**, 57-65 (1985).
62. Dicke, J., Rotermund, H.-H., & Lauterbach, J. Ellipsomicroscopy for surface imaging: contrast mechanism, enhancement, and application to CO oxidation on Pt (110). *JOSA A* **17**, 135-141 (2000).
63. Dicke, J., Erichsen, P., Wolff, J., & Rotermund, H.-H. Reflection anisotropy microscopy: improved set-up and applications to CO oxidation on platinum. *Surface science* **462**, 90-102 (2000).
64. Yuan, W. *et al.* Visualizing H_2O molecules reacting at TiO_2 active sites with transmission electron microscopy. *Science* **367**, 428-430 (2020).

65. Kresse, G., & Furthmüller, J. Efficiency of ab-initio total energy calculations for metals and semiconductors using a plane-wave basis set. *Computational material science* **6**, 15-50 (1996).
66. Kresse, G., & Furthmüller, J. Efficient iterative schemes for ab initio total-energy calculations using a plane-wave basis set. *Physical Review B* **54**, 11169 (1996).
67. Kresse, G., & Hafner, J. Ab initio molecular dynamics for liquid metals. *Physical Review B* **47**, 558 (1993).
68. Kresse, G., & Joubert, D. From ultrasoft pseudopotentials to the projector augmented-wave method. *Physical Review B* **59**, 1758 (1999).
69. Monkhorst, H. J., & Pack, J. D. Special points for Brillouin-zone integrations. *Physical Review B* **13**, 5188 (1976).
70. Perdew, J. P., Burke, K., & Ernzerhof, M. Generalized gradient approximation made simple. *Physical review letters* **77**, 3865 (1996).
71. Dannetun, H., Söderberg, D., Lundström, I., & Petersson, L.-G. The H_2–O_2 reaction on palladium studied over a large pressure range: independence of the microscopic sticking coefficients on surface condition. *Surface science* **152**, 559-568 (1985).
72. Petersson, L.-G., Dannetun, H., & Lundström, I. The water-forming reaction on palladium. *Surface science* **161**, 77-100 (1985).
73. Petersson, L.-G., Dannetun, H., & Lundström, I. Water production on palladium in hydrogen-oxygen atmospheres. *Surface science* **163**, 273-284 (1985).
74. Roques, J., Lacaze-Dufaure, C., & Mijoule, C. Dissociative adsorption of hydrogen and oxygen on palladium clusters: a comparison with the (111) infinite surface. *Journal of Chemical Theory and Computation* **3**, 878-884 (2007).

75. El-Okazy, M. A. *et al.* Gas separation performance of copolymers of perfluoro (butenyl vinyl ether) and perfluoro (2, 2-dimethyl-1, 3-dioxole). *Journal of Membrance Science* **634**, 119401 (2021).
76. Kim, K. R., Noh, J.-S., Lee, J. M., Kim, Y. J., & Lee, W. Suppression of phase transitions in Pd thin films by insertion of a Ti buffer layer. *Journal of materials science* **46**, 1597-1601 (2011).
77. Nyberg, C., & Tengstål, C. Adsorption and reaction of water, oxygen, and hydrogen on Pd (100): identification of adsorbed hydroxyl and implications for the catalytic H_2–O_2 reaction. *The Journal of chemical physics* **80**, 3463-3468 (1984).
78. Ryu, Y.-S. *et al.* Lipid membrane deformation accompanied by disk-to-ring shape transition of cholesterol-rich domains. *Journal of the American Chemical Society* **137**, 8692-8695 (2015).
79. Vaughan, J. M. *The Fabry–Perot interferometer: History, theory, practice and applications*. (Routledge, 2017).
80. Yu, E. S. *et al.* Development of a photonic switch via electro-capillarity-induced water penetration across a 10-nm gap. *Small* **18**, 2107060 (2022).
81. Baldi, A., Narayan, T. C., Koh, A. L., & Dionne, J. A. In situ detection of hydrogen-induced phase transitions in individual palladium nanocrystals. *Nature materials* **13**, 1143-1148 (2014).
82. Zhang, T., Ling, C., Xue, Q., & Wu, T. The effect of oxygen molecule on the hydrogen storage process of Li-doped graphene. *Chemical Physics Letters* **599**, 100-103 (2014).
83. Hashtroudi, H. *et al.* Hydrogen gas sensing properties of microwave-assisted 2D Hybrid Pd/rGO: Effect of temperature, humidity and UV illumination. *International Journal of Hydrogen Energy* **46**, 7653-7665 (2021).
84. Petersson, L. G., Dannetun, H. M., & Lundström, I. Hydrogen detection during catalytic surface reactions: evidence for activated lateral hydrogen

mobility in the water-forming reaction on Pd. *Physical review letters* **52**, 1806-1809 (1984).

85. Chen, H. *et al.* SERS imaging-based aptasensor for ultrasensitive and reproducible detection of influenza virus A. *Biosensors and Bioelectronics* **167**, 112496 (2020).
86. Zou, X., Wang, Y., Liu, W., & Chen, L. m-Cresol purple functionalized surface enhanced Raman scattering paper chips for highly sensitive detection of pH in the neutral pH range. *Analyst* **142**, 2333-2337 (2017).
87. Lu, Y., Liu, G. L., & Lee, L. P. High-density silver nanoparticle film with temperature-controllable interparticle spacing for a tunable surface enhanced Raman scattering substrate. *Nano letters* **5**, 5-9 (2005).
88. Lamberti, A. *et al.* Metal–elastomer nanostructures for tunable SERS and easy microfluidic integration. *RSC advances* **5**, 4404-4410 (2015).
89. Kang, M., Kim, J. J., Oh, Y. J., Park, S. G., & Jeong, K. H. A deformable nanoplasmonic membrane reveals universal correlations between plasmon resonance and surface enhanced Raman scattering. *Advanced materials* **26**, 4510-4514 (2014).
90. de Barros, A. *et al.* Dynamic behavior of surface-enhanced raman spectra for rhodamine 6G interacting with gold nanorods: Implication for analyses under wet versus dry conditions. *ACS Applied Nano Materials* **3**, 8138-8147 (2020).
91. Yang, L., Li, P., Liu, H., Tang, X., & Liu, J. A dynamic surface enhanced Raman spectroscopy method for ultra-sensitive detection: from the wet state to the dry state. *Chemical Society Reviews* **44**, 2837-2848 (2015).
92. Dang, H. *et al.* Reproducible and sensitive plasmonic sensing platforms based on Au-nanoparticle-internalized nanodimpled substrates. *Advanced Functional Materials* **31**, 2105703 (2021).
93. Shin, D. Organic vapor-modulated surface enhanced Raman scattering spectroscopy. *RSC advances* **6**, 58694-58697 (2016).

94. Shoute, L. C. T., Bergren, A. J., Mahmoud, A. M., Harris, K. D., & McCreery, R. L. Optical interference effects in the design of substrates for surface-enhanced Raman spectroscopy. *Applied spectroscopy* **63**, 133-140 (2009).
95. Guo, Y. *et al.* Using a Fabry–Perot cavity to augment the enhancement factor for surface-enhanced Raman spectroscopy and tip-enhanced Raman spectroscopy. *The Journal of Physical Chemistry C* **122**, 14865-14871 (2018).
96. Sun, X., & Li, H. Gold nanoisland arrays by repeated deposition and post-deposition annealing for surface-enhanced Raman spectroscopy. *Nanotechnology* **24**, 355706 (2013).
97. Shevchenko, A., Ovchinnikov, V., & Shevchenko, A. Large-area nanostructured substrates for surface enhanced Raman spectroscopy. *Applied Physics Letters* **100**, 171913 (2012).
98. Schmidt, M. S., Hübner, J., & Boisen, A. Large area fabrication of leaning silicon nanopillars for surface enhanced raman spectroscopy. *Advanced Materials* **24**, OP11-OP18 (2012).
99. Park, S. G. *et al.* Surface energy-controlled SERS substrates for molecular concentration at plasmonic nanogaps. *Advanced Functional Materials* **27**, 1703376 (2017).
100. Choy, T. C. *Effective medium theory: Principles and applications*, vol. 165. (Oxford University Press, 2015).
101. Zhou, H. *et al.* Trinitrotoluene explosive lights up ultrahigh Raman scattering of nonresonant molecule on a top-closed silver nanotube array. *Analytical chemistry* **83**, 6913-6917 (2011).
102. Lee, S. *et al.* Utilizing 3D SERS active volumes in aligned carbon nanotube scaffold substrates. *Advanced Materials* **24**, 5261-5266 (2012).

103. Prieto, M. J. *et al.* Water formation under silica thin films: real-time observation of a chemical reaction in a physically confined space. *Angewandte Chemie International Edition* **57**, 8749-8753 (2018).
104. Ngene, P. *et al.* Seeing hydrogen in colors: low-cost and highly sensitive eye readable hydrogen detectors. *Advanced Functional Material* **24**, 2374-2382 (2014).
105. Duan, X., Kamin, S., & Liu, N. Dynamic plasmonic colour display. *Nature communications* **8**, 14606 (2017).
106. Shalabney, A. *et al.* Enhanced raman scattering from vibro-polariton hybrid states. *Angewandte Chemie International Edition* **127**, 8082-8086 (2015).
107. Wang, Y. *et al.* Sharp phase variations from the plasmon mode causing the Rabi-analogue splitting. *Nanophotonics* **6**, 1101-1107 (2017).
108. Ameling, R., & Giessen, H. Microcavity plasmonics: strong coupling of photonic cavities and plasmons. *Laser & photonics reviews* **7**, 141-169 (2013).
109. Konrad, A. *et al.* Manipulating the excitation transfer in photosystem I using a Fabry–Perot metal resonator with optical subwavelength dimensions. *Physical Chemistry Chemical Physics* **16**, 6175-6181 (2014).
110. Badiya, P. K. *et al.* Ag-protein plasmonic architectures for surface plasmon-coupled emission enhancements and Fabry-Perot mode-coupled directional fluorescence emission. *Chemical Physics Letters* **685**, 139-145 (2017).
111. Li, D., Tang, L., Wang, J., Liu, X., & Ying, Y. Multidimensional SERS barcodes on flexible patterned plasmonic metafilm for anticounterfeiting applications. *Advanced Optical Materials* **4**, 1475-1480 (2016).
112. Liu, Y., Lee, Y. H., Lee, M. R., Yang, Y., & Ling, X. Y. Flexible three-dimensional anticounterfeiting plasmonic security labels: utilizing z-axis-

dependent SERS readouts to encode multilayered molecular information. *ACS Photonics* **4**, 2529-2536 (2017).

113. Gu, Y., He, C., Liu, F., & Ye, J. Raman ink for steganography. *Advanced Optical Materials* **9**, 2002038 (2021).
114. Lee, H. *et al.* Surface plasmon localization-based super-resolved Raman microscopy. *Nano letters* **20**, 8951-8958 (2020).
115. Nam, W. *et al.* Plasmonically calibrated label-free surface-enhanced Raman spectroscopy for improved multivariate analysis of living cells in cancer subtyping and drug testing. *Analytical Chemistry* **93**, 4601-4610 (2021).
116. Zheng, Y. *et al.* Reversible gating of smart plasmonic molecular traps using thermoresponsive polymers for single-molecule detection. *Nature communications* **6**, 8797 (2015).

Publications

Journals

1. **J. Lee**, E.-S. Yu, T. Kim, I. S. Kim, J. Kwak, S. Chung, S. J. Kwak, W. B. Lee, Y. Pak, and Y.-S. Ryu, "Naked-eye observation of water-forming reaction on palladium etalon: transduction of gas-matter reaction into light-matter", Accepted, *PhotoniX*.
2. T. Kim†, **J. Lee**†, E.-S. Yu, S. Lee, H. Woo, J. Kwak, S. Chung, I. Choi and Y.-S. Ryu, "Fabry-Perot cavity control for tunable Raman scattering", *Small*, Early View, 2207003, 2023.
3. E.-S. Yu, K. Chae, T. Kim, **J. Lee**, J. Seo, I. S. Kim, A. J. Chung, S.-D. Lee, and Y.-S. Ryu, "Development of a photonic switch via electro-capillarity-induced water penetration across a 10-nm gap", *Small*, 18, 2107060, 2022.
4. H.-D. Jeong†, **J. Lee**†, E.-S. Yu, T. Kim, I. S. Kim, S.-D. Lee, Y.-S. Ryu, and S.-Y. Lee, "Physicochemical modulation of nanometer-thick etalon films for liquid-sensitive color display with full-color spectrum generation", *ACS Applied Nano Materials*, 4, 389–395, 2020.
5. Y. Kim, E.-S. Yu, Y.-G. Bae, **J. Lee**, I. S. Kim, S. Chung, S.-Y. Lee, and Y.-S. Ryu, "Asymmetric optical camouflage: tuneable reflective colour accompanied by the optical Janus effect", *Light Science & Applications*, 9, 175, 2020.

6. E.-S. Yu, H. Lee, S.-M. Lee, J. Lee, T. Kim, **J. Lee**, C. Kim, M. Seo, J. H. Kim, Y. T. Byun, S.-C. Park, S.-Y. Lee, S.-D. Lee, and Y.-S. Ryu, “Precise capture and dynamic relocation of nanoparticulate biomolecules through dielectrophoretic enhancement by vertical nanogap architectures”, *Nature Communications,* 11, 2804, 2020.

Patents

1. Y.-S. Ryu, Y. Pak, **J. Lee**, T. Kim, E.-S. Yu, “Hydrogen sensing device that can visually detect the presence of hydrogen through color change according to the water formation reaction”, US 18/107763 (Application)
2. 유용상, 김태현, **이종수**, 유의상, 정의태, “라만산란신호의 세기를 선택적으로 조절할 수 있는 SERS 기판 및 그 제조방법”, KR 10-2022-0090168 (출원).
3. 유용상, 박유신, **이종수**, 김태현, 유의상, “물 형성 반응에 따른 색변화를 통해 수소의 존재를 시각적으로 감지할 수 있는 수소감지장치”, KR 10-2022-0090169 (출원).
4. 유용상, 우덕하, 유의상, **이종수**, 박유신, 서민아, 김철기, 송현석, 이택진, 전명석, 전영민, 변영태, 이석, 김재헌, “입자 포집 장치 및 입자 센싱 방법”, KR 10-2020-0096819 (출원), KR 10-2362856 (등록).
5. 유용상, 유의상, **이종수**, 백지민, 박유신, 서민아, 송현석, 변영태, 전명석, 이택진, 전영민, 우덕하, 이석, 김철기, 김재헌, “독립형 부유 전극 구조의 입자 포집 장치 및 이를 이용한 입자 포집 방법”, KR 10-2020-0096818 (출원), KR 10-2443561 (등록).
6. 유용상, 김상문, 유의상, 김태현, **이종수**, “수직 나노갭 전극을 구비한 미세먼지 포집용 필터 및 이를 이용한 미세먼지 저감 장치 및 방법”, KR 10-2020-0096663 (출원), KR 10-2347063 (등록).

Abstract (In Korean)

빛과 물체 간의 상호작용은 귀금속 나노 구조체를 기반에서 매우 독특한 광학 특성을 보이고, 이는 상용화 소자 개발뿐 아니라 과학적 발견에 상당한 잠재력이 있어 꾸준한 관심을 받아 왔다. 한편, 실생활에 응용 가능한 수준의 넓은 폭의 색을 구현하기 위한 나노 구조 플랫폼을 제작하는 것은 고비용과 복잡한 제조 과정이 요구된다. 이러한 관점에서 패브리-페로 광공진기는 직관적이고 다용도의 광학 구조로써 유전체 공간에 가둬진 광자 물질과 반응하여 넓은 파장 범위에서의 공명을 일으키는 빛-물체 간 상호작용이 일어난다. 에탈론 이라고 알려진 금속-유전체-금속의 얇은 박막 적층 구조는 가시 영역에서 모든 색을 구현 가능한 패브리-페로 간섭현상을 일으키고, 각 구성층의 구조와 물질을 설계하여 높은 수준의 색 조율이 가능하다. 이는 상대적으로 비용 효율이 높아 대면적, 대량 생산에 유리한 증착과 스핀코팅 공정을 필요로 한다.

우선, 각 구성 박막의 두께와 충만 분획을 정밀하게 재단하여 섬세한 색 차이를 만들어 내고, 이론적 모델링을 통해 색깔 안내에 있어 제한 기준을 확립하였다. 구체화된 실험을 통해 나노 구조를 갖은 박막 에탈론을 만들어 고유의 구조 색 발현을 보여주었고, 색 조정 능력을 적용하여 주변 환경에 반응하여 모습을 위장하는 기능

모사를 하였다. 둘째로, 기체와 물체 간의 상호작용을 빛-물체 간의 작용으로 변환시켜 팔라듐 표면에서의 기체 흡탈착 거동을 시각화하고자 하였다. 팔라듐은 기체 산업에서 수소의 저장, 정화, 검출, 촉매와 같이 폭넓은 분야에 사용되는 가장 중요한 물질로써, 수소 촉매와 흡수물질로써 독보적인 특성을 갖고 있다. 그리하여, 팔라듐을 에탈론의 상하부 금속제로 이용한다면 일반 대기에서 기체 농도에 따라 노출 기체와의 반응을 색 변화 반응으로 보여주고, 유전체와 팔라듐 계면에서 발생하는 물 형성 반응 또한 육안으로 볼 수 있는 색 변화로 만들 수 있다. 이러한 소자를 성공적으로 만들어 보였고, 기체 누출 경보 시스템으로의 응용 가능한 수준을 보였다. 마지막으로, 에탈론 구조를 최신 분자 검지 기술에 적용하여 표면 강화 라만 산란의 강화 지수를 조정하는 라만 스위치로 사용하였다. 컴퓨터 계산 분석과 실험적 분석을 통해 패프리-페로 에탈론을 구성하는 나노 구조를 설계하여 최대의 장거리장 강화 지수와 근거리장을 만들어 내는 조건을 조사하였다. 이러한 광공진기의 구조적 특성을 변화하여 표면 강화 라만 산란을 조정하는 것은 정보 암호화에도 응용된다.

결론적으로, 이 학위 논문은 박막 광소자로써 금속-유전체-금속 에탈론 구조를 전체에 걸쳐 조사하고 이를 광학뿐 아니라 표면 화학, 비균질 촉매반응, 생체 모방, 분자 분석과 같은 다양한 응용 분야를 제안한다. 실험적 분석과 컴퓨터 계산 분석을 모두

진행하여 에탈론 소자의 구성 성분과 나노 형태에 따라 소자의 광학적 거동을 증명하였다. 금속–유전체–금속 구조 안에 역학성을 도입하는 전략은 더 넓은 범위의 파장 스펙트라를 위해 다양한 광자 나노 구조에도 적용할 수 있다.

주요어: 페브리-페로 에탈론, 구조색, 물 형성 반응, 색채계 센서, 라만 분광법

학번: 2018-35203